Multi-Model Intercomparison of the Pan-Arctic Ice-Algal Productivity on Seasonal, Interannual, and Decadal Timescales

Eiji Watanabe, Meibing Jin, Hakase Hayashida, Jinlun Zhang & Nadja Steiner

October 2019

JGR Oceans
RESEARCH ARTICLE
10.1029/2019JC015100

Special Section:
Forum for Arctic Modeling and Observational Synthesis (FAMOS) 2: Beaufort Gyre phenomenon

Multi-Model Intercomparison of the Pan-Arctic Ice-Algal Productivity on Seasonal, Interannual, and Decadal Timescales

Eiji Watanabe[1], Meibing Jin[2,3,4], Hakase Hayashida[5,6], Jinlun Zhang[7], and Nadja Steiner[8]

[1]Japan Agency for Marine-Earth Science and Technology, Yokosuka, Kanagawa, Japan, [2]School of Marine Sciences, Nanjing University of Information Science and Technology, Nanjing, China, [3]Southern Laboratory of Ocean Science and Engineering, Zhuhai, China, [4]International Arctic Research Center, University of Alaska Fairbanks, Fairbanks, AK, USA, [5]School of Earth and Ocean Sciences, University of Victoria, Victoria, British Columbia, Canada, [6]Institute for Marine and Antarctic Studies, University of Tasmania, Hobart, Tasmania, Australia, [7]Polar Science Center, University of Washington, Seattle, WA, USA, [8]Fisheries and Oceans Canada, Institute of Ocean Sciences, Sidney, British Columbia, Canada

Key Points:
- An appropriate balance of stable sea-ice cover and enough light availability is necessary to retain ice-algal productivity
- Annual total ice-algal productivity has no common decadal trend for 1980–2009 among the five marine ecosystem models
- The multi-model averages show that ice-algal bloom timing shifts to an earlier date and the bloom duration shortens in four subregions

Correspondence to:
E. Watanabe,
ejnabe@jamstec.go.jp

Citation:
Watanabe, E., Jin, M., Hayashida, H., Zhang, J., & Steiner, N. (2019). Multi-Model Intercomparison of the Pan-Arctic Ice-Algal Productivity on Seasonal, Interannual, and Decadal Timescales. *Journal of Geophysical Research: Oceans*, *124*, 9053–9084. https://doi.org/10.1029/2019JC015143

Received 26 FEB 2019
Accepted 10 OCT 2019
Accepted article online 24 OCT 2019
Published online 16 DEC 2019

Abstract Seasonal, interannual, and decadal variations in the Arctic ice-algal productivity for 1980–2009 are investigated using daily outputs from five sea ice-ocean ecosystem models participating in the Forum for Arctic Modeling and Observational Synthesis project. The models show a shelf-basin contrast in the spatial distribution of ice-algal productivity (ice-PP). The simulated ice-PP substantially varies among the four subregions (Chukchi Sea, Canada Basin, Eurasian Basin, and Barents Sea) and among the five models, respectively. The simulated annual total ice-PP has no common decadal trend at least for 1980–2009 among the five models in any of the four subregions, although the simulated snow depth and sea-ice thickness in spring are mostly declining. The model intercomparison indicates that an appropriate balance of stable ice-algal habitat (i.e., sea-ice cover) and enough light availability is necessary to retain the ice-PP. The multi-model averages show that the ice-algal bloom timing shifts to an earlier date and that the bloom duration shortens in the four subregions. However, both the positive and negative decadal trends in the timing and duration are simulated. This difference in trends are attributed to temporal shifts among different types of ice-algal blooms: long-massive, short-massive, long-gentle, and short-gentle bloom. The selected value for the maximum growth rate of the ice-algal photosynthesis term is a key source for the inter-model spreads. Understanding the simulated uncertainties on the pan-Arctic and decadal scales is expected to improve coupled sea ice-ocean ecosystem models. This step will be a baseline for further modeling/field studies and future projections.

1. Introduction

Responses of the marine biogeochemical cycle to the Arctic sea-ice decline have become an important topic for a variety of scientific, social, and economic communities. Primary production (PP) of phytoplankton is suggested to continuously increase associated with the reduction in sea-ice extent over the Arctic shelves (Arrigo & van Dijken, 2015) as long as nutrients are available (Tremblay et al., 2015). Sea-ice algae are also important for the biological pump of CO_2, because the sinking of ice-algal assemblages to the deep seafloors is considered to be much faster than that of pelagic plankton species (Boetius et al., 2013). Ice algae are an essential food source for zooplankton and benthos in the marginal sea-ice zone (Michel et al., 1996; Schollmeier et al., 2018). Generally, sea-ice decline plays increasing and decreasing roles in ice-algal biomass. Snow and sea-ice thinning enhances light penetration into the skeletal layer at the sea ice-ocean interface. On the other hand, reduction in net thermal ice growth (i.e., freezing minus melting) restricts nutrient availability due to dilution with fresh meltwater and a corresponding more-stratified surface layer. Ice-algal habitat itself is lost directly by the shrinking of sea-ice area. Therefore, impacts of sea-ice decline on ice-algal productivity should be evaluated from multiple views covering the pan-Arctic region on decadal timescales.

Numerical modeling is a powerful tool to estimate the impacts of sea-ice decline on ice-algal productivity and identify the relative contribution of physical and biogeochemical factors. Sea-ice ecosystem models have a long history of development. Most previous works have been conducted on one-dimensional landfast ice fields in the Antarctic (Arrigo et al., 1993), Lake Saroma of Hokkaido, Japan (Nishi & Tabeta, 2005), Canadian Arctic Resolute (Lavoie et al., 2005; Mortenson et al., 2017), and Point Barrow north of Alaska (Jin et al., 2006). According to these studies, the complicated ice-algal processes have been numerically formulated in various ways. In recent years, the model domains extended from a single landfast ice station to the pan-Arctic scale (Castellani et al., 2017; Deal et al., 2011; Hayashida et al., 2019; Watanabe et al., 2015). Decadal simulations in the three-dimensional framework are also performed by several research groups. Dupont (2012) set up a pan-Arctic regional modeling for 1950–2006 and estimated that the relative contribution of ice algae to total PP could be 40% in the central Arctic Ocean. A global model experiment provided annual total ice-algal production of 21.3 Tg C in the Northern Hemisphere for 1998–2007 (cf. phytoplankton production of 413 $\pm$ 88 Tg C in the uppermost 100 m within the Arctic Circle) (Jin et al., 2012). These decadal simulations enabled statistical analyses on interannual variability in sea-ice area and ice-algal productivity. For example, Dupont (2012) indicates that extensive sea-ice area is preferable for ice-algal activity, based on a positive correlation between September ice cover and yearly ice-algal production in the Arctic Ocean. Conversely, sea-ice decline sometimes enhances the productivity, since a correlation between annual averages of the pan-Arctic sea-ice area and ice-algal production was negative in Jin, Deal, et al. (2012). As shown in these studies, ice-algal sensitivity to sea-ice cover is highly variable due to combined effects of light intensity and nutrient availability at the sea ice-ocean interface.

The Arctic Ocean Model Intercomparison Project (AOMIP) and a subsequent Forum for Arctic Ocean Modeling and Observational Synthesis (FAMOS) project have provided opportunities to capture the present status and uncertainty of global and pan-Arctic sea ice-ocean models (Proshutinsky et al., 2016). The first intercomparison of marine ecosystem models including the entire Arctic Ocean revealed that nutrient availability in the euphotic zone associated with surface mixed-layer depths was a crucial factor for inconsistencies in pelagic PP for the five models tested (Popova et al., 2012). The assessment of 21 models with an in situ biogeochemical database for 1959–2011 indicated that the model skill of PP was greater in the central Arctic basin than in the shallow shelves (Lee et al., 2016). Both studies reported biases of the simulated sea-ice cover and ocean nitrate. An intercomparison with three models suggested that the relative contribution of the under-ice bloom to the annual total PP were correlated with the duration of the sea-ice cover in several Arctic regions and on a decadal timescale (Jin et al., 2016). The subsurface Chl-*a* maximum (SCM) in the Canada Basin was compared among six Earth System Models (ESMs) participating in the 5th Coupled Model Intercomparison Project (CMIP5) and three sea ice-ocean models (Steiner et al., 2016). Whereas a few models simulating anomalous nutrients in the ocean surface layer failed to represent the SCM, most models produced the nutricline and SCM deepening due to the enhanced wind-driven Ekman convergence in a future climate scenario. Vancoppenolle, Bopp, et al. (2013) revealed that disagreement of the future PP trend in the water column projected by the 11 CMIP5 models was attributed to intermodel spread of nitrate availability. More recently, a non-linear response of the ice-algal phenology to the CMIP5-derived physical variables was projected under warming climate in a sea-ice biogeochemical model (Tedesco et al., 2019).

In the present study, a multi-model intercomparison of Arctic ice-algal productivity is conducted as a subject of the FAMOS Phase II biogeochemical working group (https://famosarctic.com/index.html). The main purpose of this intercomparison is to estimate potential uncertainties of the ice-algal productivity and to explore controlling factors for variability of the ice-algal productivity on seasonal, interannual, and decadal timescales. Simulated variables for 1980–2009 are analyzed in four subregions: Chukchi Sea, Canada Basin, Eurasian Basin, and Barents Sea. Net primary production of ice algae (i.e., photosynthesis minus respiration) is referred to as ice-PP, hereafter. Configuration and experimental design of the five models developed in Japan, Canada, and the United States are described in section 2. The pan-Arctic spatial distributions of the simulated ice-PP, sea-ice thickness, and nitrate concentrations in the ocean surface layer are compared in section 3. Seasonal transitions in the ice-PP and potential key factors in the four subregions are investigated in section 4. The analysis extends to interannual and decadal variability in section 5. The bloom timing and duration are discussed in section 6. The obtained findings and future perspective are summarized in section 7.

2. Model Configuration and Experimental Design

The present study analyzed daily outputs of five models developed in the Japan Agency for Marine-Earth Science and Technology (JAMSTEC), the University of Alaska Fairbanks (UAF), the University of Victoria (UVic), and the University of Washington (UW). Two packages of global and regional versions are provided by the UAF. The other three data sets are produced by pan-Arctic regional models. Model configuration, grid size, atmospheric forcing, initial nutrient conditions, and major ecosystem variables are listed in Tables 1 and 2. More details are described in the following subsections. For reference, previous versions of the UAF and UW models participated in multi-model intercomparison studies of pelagic primary productivity (Lee et al., 2016; Popova et al., 2012).

2.1. The JAMSTEC Model

The Arctic and North Pacific Ecosystem Model for Understanding Regional Oceanography (Arctic NEMURO) is developed at the JAMSTEC (Watanabe et al., 2015). The detailed configuration of the original NEMURO model, which represents three nutrients (nitrate, ammonium, and silicate), five pelagic plankton groups (diatoms, flagellates, micro-zooplankton, copepod, and predator zooplankton), dissolved organic nitrogen, particulate organic nitrogen (PON), and opal (OPL), is described in Kishi et al. (2007). The latest version of the Arctic NEMURO includes ice algae, ice-related fauna, and faster-sinking biogenic particles derived from the sea-ice ecosystem (fPON and fOPL) (Watanabe et al., 2015). The physical part of the coupled sea ice-ocean model is the Center for Climate System Research Ocean Component Model (COCO) version 4.9 (Hasumi, 2006). The sea-ice component adopts a seven category distributions of sub-grid snow depth and sea-ice thickness with a one-layer thermodynamic formulation (Bitz et al., 2001; Bitz & Lipscomb, 1999; Lipscomb, 2001) and elastic-viscous-plastic (EVP) rheology (Hunke & Dukowicz, 1997).

The model and experimental design follow Watanabe et al. (2014, 2015) except for the grid size and integration period. The model domain covers the entire Arctic Ocean, the Nordic seas, and the North Atlantic north of 45°N. The model is configured in the spherical coordinate system rotated by 90° so that the singular points (i.e., the North and South Poles of the model grid) are located at the equator. The horizontal resolution is 1/4° (approximately 25 km) in the rotated coordinate. This configuration is composed of 280 × 200 horizontal grid points and 28 vertical levels. The layer thickness varies from 2 m in the uppermost layer to 500 m below 1,000 m depth.

The spin-up experiment initiated with no sea ice, no ocean current, and temperature and salinity fields of the Polar Science Center Hydrographic Climatology (PHC) version 3.0 (Steele et al., 2001) is conducted for 10 years under the atmospheric conditions in 1979. The decadal experiment from 1979 to 2013 is then performed. The atmospheric forcing components are constructed from the Climate Forecast System Reanalysis (CFSR: 1979–2010) and version 2 (CFSv2: 2011–2013) 6 hourly data set of the National Centers for Environmental Prediction (NCEP) (Saha et al., 2010) (hereafter, CFSR). The Bering Strait throughflow is given by idealized seasonal cycles of velocity, temperature, and salinity based on Woodgate et al. (2005). The monthly climatology data of nitrate and silicate concentrations from the World Ocean Atlas 2013 (WOA13) (Garcia et al., 2013) are used for a restoring along the lateral boundary region of the model domain, and the winter climatology is assigned for the initial fields of ocean nutrients in 1979. Sea-ice nutrients are initially non-existent in the skeletal layer, and the lowest ice-algal concentration of 0.02 mmol N m^{-3} is given for seeding.

2.2. The University of Alaska Fairbanks (UAF-G, UAF-R) Models

The UAF simulations are based on a common marine biogeochemical module (Jin, Deal, et al., 2012; Moore et al., 2004), which is incorporated into the global Community Earth System Model (CESM) (Moore et al., 2013) and the Regional Arctic System Model (RASM) (http://www.oc.nps.edu/NAME/RASM_PhaseIII.html), respectively. The detailed model configuration and experimental design of both the global and regional frameworks were introduced in Jin et al. (2018). The sea-ice ecosystem consists of ice algae and three nutrients (nitrate, ammonium, and silicate) (Jin et al., 2006). The pelagic variables include three phytoplankton groups (diatoms, flagellates, and diazotrophs), one zooplankton group, and four nutrients (nitrate, ammonium, phosphate, and silicate). The physical component is the Parallel Ocean Program (POP)-CICE model originally developed at the Los Alamos National Laboratory. A sea-ice module with five thickness categories and four-layer thermodynamics is adopted (Bitz & Lipscomb, 1999). The RASM developed at

Table 1
Experimental Information of the JAMSTEC, UAF-G, UAF-R, UVic, and UW Models

		JAMSTEC	UAF-G	UAF-R	UVic	UW
Physics		COCO	CESM	RASM	NEMO	PIOMAS
Ecosystem	Ice	Watanabe et al. (2015)	Jin et al. (2006)	Jin et al. (2006)	Hayashida (2018)	Jin et al. (2006)
	Ocean	NEMURO[a]	Moore et al. (2013)	Moore et al. (2013)	CanOE	NEMURO[a]
Domain		Pan-Arctic[b] (45–90°N)	Global	Pan-Arctic (30–90°N)	Pan-Arctic[c] (45–90°N)	Pan-Arctic (39–90°N)
Grid size (H)		25 km	18–85 km	9 km	10–15 km	2–80 km
Grid size (V)		2–500 m (28 layers)	10–250 m (60 layers)	5–250 m (45 layers)	1–255 m (46 layers)	5–600 m (40 layers)
Atom. forcing		NCEP-CFSR	CORE II	CORE II	DFS	NCEP-CFSR
Initial nutrient		WOA13	WOA13	WOA13	GLODAPv2	WOA05
Reference		Watanabe et al. (2015)	Jin et al. (2018)	Jin et al. (2018)	Hayashida (2018)	Zhang et al. (2015)

[a]NEMURO model was upgraded at JAMSTEC and UW, respectively [b]Only north of Bering Strait in Pacific side. [c]Only north of Bering Sea in Pacific side.

the Naval Postgraduate School added several adjustments such as a brine-rejection parameterization (Jin, Hutchings, et al., 2012), explicit level-ice ponds (Hunke et al., 2013), the elastic-anistropic-plastic sea-ice rheology (Wilchinsky & Feltham, 2004).

The global version based on the CESM framework (named "UAF-G," hereafter) is composed of 320 × 384 horizontal grid points, where the North Pole of the model grid is moved to Greenland. The Northern Hemisphere grid size ranges from 18 km along the Greenland coast to 62 km at the Bering Strait and 85 km at the equator. The vertical grid consists of 40 levels whose thickness varies from 10 to 250 m. The regional version based on the RASM framework (named "UAF-R," hereafter) is composed of 1,280 × 720 grid points north of 30°N, where the North Pole of the model grid is located at the equator. The horizontal resolution is 1/12° (approximately 9 km) in the rotated spherical coordinate. There are 45 vertical layers whose thickness ranges from 5 to 250 m.

After spin-up experiments for 1965–1974 initiated with no ocean current, both the global and regional models were integrated from 1975 to 2009, driven by atmospheric forcing data of the Coordinated Ocean-ice Reference Experiments Phase II (CORE II) (Large & Yeager, 2009). The initial fields are obtained from the PHC3.0 (Steele et al., 2001) for temperature and salinity, the WOA13 (Garcia et al., 2013) for nitrate and silicate concentrations, and a previous CESM simulation (Moore et al., 2013) for other biogeochemical constituents. Temperature and salinity along the RASM lateral boundaries are restored to the PHC monthly climatology.

2.3. The UVic Model

The sea-ice ecosystem model used at the UVic is the Canadian Sea-ice Biogeochemistry model version 1 (CSIB v1) coupled with a modified version from the Canadian Ocean Ecosystem model (CanOE) (Hayashida et al., 2019). The sea-ice ecosystem consists of ice algae, nitrate, and ammonium (Hayashida et al., 2017; Mortenson et al., 2017). CanOE is developed at the Canadian Centre for Climate Modelling

Table 2
Major Ecosystem Variables of the JAMSTEC, UAF-G, UAF-R, UVic, and UW Models

	JAMSTEC	UAF-G	UAF-R	UVic	UW
Ice algae (IA)	1	1	1	1	2
Ice-related fauna	—[a]	—	—	—	—
Phytoplankton	2	3	3	2	2
Zooplankton	3	1	1	2	3
Nutrient	NO_3, NH_4, Si	NO_3, NH_4, PO_4, Si	NO_3, NH_4, PO_4, Si	NO_3, NH_4	NO_3, NH_4, Si
Iron limitation for IA	No	No	No	No	No
Dissolved organic matter	DON	DOC	DOC	—	DON
Particulate organic matter	fPON, sPON	POC	POC	small POC, large POC	PON

[a]Included in the model formulation, but its biomass is kept at zero.

and Analysis for the latest version of the Canadian Earth System Model (Arora et al., 2011) and simulates lower-trophic level pelagic ecosystem (two phytoplankton and two zooplankton groups) and biogeochemical cycling of key elements (e.g., nitrogen and carbon) (Hayashida, 2018). The physical component is the Nucleus for European Modeling of the Ocean (NEMO) numerical framework version 3.4 including the Océan PArallélisé (OPA) (Madec, 2008) and the Louvain-la-Neuve sea-ice model version 2 (LIM2) (Fichefet & Maqueda, 1997). LIM2 adopts a two-layer thermodynamic scheme and the EVP rheology.

The model domain and resolution are based on the North Atlantic and Arctic (NAA) configuration developed at the University of Alberta (Hu & Myers, 2013). The NAA domain covers the northern Bering Sea, the Arctic Ocean, the Nordic seas, and a part of the North Atlantic (>45°N). The horizontal resolution of 568 × 400 grid points varies from 10 km along the North American boundary to 14.5 km along the Eurasian boundary in a curvilinear orthogonal coordinate system. The ocean is divided into 46 vertical levels with variable thickness of 1–255 m. The vertical resolution in the upper layers is finer than that of the original NAA configuration.

The hydrographic variables are initialized from rest with temperature and salinity fields in January 1969, which are derived from the Ocean Reanalysis System version 4 (ORAS4) (Balmaseda et al., 2013). The initial snow depth, sea-ice thickness, and sea-ice concentration are set to 0.1 m, 2.5 m, and 0.95, respectively, for grid cells where sea surface temperature anomaly from the seawater freezing point is within 2 °C. Elsewhere, these values are set to zero. The initial nitrate concentration is constructed from a gridded composite field of the Global Ocean Data Analysis Project version 2 (GLODAPv2) (Lauvset et al., 2016). The initial concentrations of sea-ice biogeochemical variables are set to the same values as those in the uppermost ocean layer. After a spin-up experiment for 1969–1978, the model is integrated from 1979 to 2015. The atmospheric conditions are obtained from the Drakkar Forcing Set (DFS) version 5.2 (Dussin et al., 2016) based on a blend of the ERA-40 and ERA-Interim reanalysis products (Dee et al., 2011; Uppala et al., 2005). Open boundary conditions with the monthly mean horizontal ocean velocity, temperature, and salinity fields of the ORAS4 are applied using a radiation-relaxation algorithm (Madec, 2008) in the Bering Sea and the North Atlantic. The boundary conditions for marine biogeochemical variables are the same as their initial conditions.

2.4. The University of Washington (UW) Model

The coupled pan-Arctic Biology-Ice-Ocean Modeling and Assimilation System (BIOMAS) developed at the UW has a pelagic ecosystem model modified from the original NEMURO (Kishi et al., 2007). The model configuration and experimental design follow Zhang et al. (2010, 2015), whereas their previous experiments did not include sea-ice biogeochemistry. The sea-ice ecosystem has two ice algae groups (i.e., diatoms and flagellates) with three nutrients (nitrate, ammonium, and silicate). Exchange of biogeochemical variables at the sea ice-ocean interface is formulated as in Jin et al. (2006). The physical ocean model is the modified POP (Zhang & Steele, 2007). The sea-ice scheme is formulated with eight category distributions of snow depth, sea-ice thickness, and sea-ice enthalpy (Zhang & Rothrock, 2003). The assimilation option of satellite-based sea-ice concentration and sea surface temperature (Schweiger et al., 2011) is also applied.

The model domain covers the Northern Hemisphere north of 39°N. The generalized orthogonal curvilinear coordinate system has a horizontal dimension of 600 × 300 grid points. The North Pole of the BIOMAS grid is placed in Alaska so that the model has its highest horizontal resolution in the Chukchi, Beaufort, and Bering seas. The model resolution averaged in the Alaskan coastal area is approximately 4 km. There are 40 vertical levels whose layer thickness ranges from 5 to 600 m. The ocean velocity, temperature, salinity, and sea surface height from the Global Ice-Ocean Modeling and Assimilation System (GIOMAS) (Zhang & Rothrock, 2003) are used as open boundary conditions for the southern edges of the model domain. In addition, nitrate and silicate concentrations along the open boundaries are restored to the World Ocean Atlas 2005 (WOA05) monthly climatology (Garcia et al., 2006).

The model is integrated from 1979 to 2016, driven by the CFSR atmospheric forcing. The initial conditions of sea-ice and ocean variables in 1979 are obtained from the GIOMAS integration starting from 1948 (Zhang & Rothrock, 2003) and the January climatology fields of the WOA05 nitrate and silicate concentrations. The initial conditions of other biogeochemical variables in the upper 200 m are given by a uniform distribution (0.02 mmol N m^{-3}; 0.02 mmol Si m^{-3}).

2.5. Overview of Ice Algae Model and Experimental Design

The ice-algal biomass budget in the five models is mostly composed of (1) photosynthesis, (2) respiration, (3) mortality, (4) excretion, (5) zooplankton grazing, (6) meltwater-induced release from the skeletal layer, and (7) lateral advection. In the present study, (1) and (2) are combined as the ice-PP. The sink terms of (3)–(6) and the lateral advection are not directly compared in the present study. The photosynthesis term per unit biomass is formulated with a maximum growth rate (V_{maxi}) multiplied by limitation factors of light and nutrient. The V_{maxi} value of 1.2 day^{-1} in the JAMSTEC model is based on a collaborative study with mooring measurements around the Chukchi Borderland (unpublished). 1.44 day^{-1} in the UAF-G and UAF-R models, 0.85 day^{-1} in the UVic model, and 4.0 day^{-1} in the UW model are derived from Jin et al. (2006), Lavoie et al. (2005), and Gradinger (2009), respectively. Light intensity at the skeletal layer is given by downward shortwave radiation from atmosphere, snow/ice surface albedo, snow depth, sea-ice thickness, and empirical extinction rates. In the JAMSTEC model, horizontal scattering of shortwave radiation absorbed by open leads contributes to the light availability, and a strong light inhibition is applied to ice algae as well as pelagic phytoplankton (Kishi et al., 2007). The five models commonly employ the Michaelis-Menten function for the nutrient limitation factor. The JAMSTEC model applies nutrient entrainment due to sea-ice freezing, instead of vertical diffusive fluxes, and a hybrid uptake of sea ice and ocean surface nutrients (Watanabe et al., 2015). Multi-layer habitats, sediment shading, salinity stress, and iron limitation proposed in previous studies (e.g., Vancoppenolle, Meiners, et al., 2013) might also be important for the ice-PP but are not incorporated in any of the five models.

In general, the simulated spatial distribution of ocean nutrients is strongly influenced by the horizontal resolution, as indicated in a previous intercomparison between two versions of the UAF models (Jin et al., 2018). The coarser-resolution models occasionally cause excessive numerical diffusion of shelf-origin nutrient-rich water toward the central basin. There is a difference in the nutrient data set for initial condition (Table 1). Since the gridded composite field of the GLODAPv2 product includes missing values especially in the central basin and the deeper layers, spatial interpolation was applied for the UVic experiment. Whereas we do not judge which data set is more preferable for our experiments in the present study, the impact of the initial nutrient difference would be much smaller than that in the CMIP5 simulations after >1,000-year spin-up (Vancoppenolle, Bopp, et al., 2013). Besides, it should be noted that in the JAMSTEC model, nutrient restoring to the WOA13 monthly climatology at the Bering Strait dampens the interannual and decadal variability in the western Arctic. Similarly, the UVic model has a lateral boundary in the Bering Sea, where the nitrate concentration is prescribed to the GLODAPv2 annual climatology. Since atmospheric forcing components for the sea ice-ocean models (Table 1) are derived from the reanalysis data sets (i.e., NCEP-CFSR, CORE II, and DFS), which reflect the satellite-based sea-ice concentration (SIC), the simulated sea-ice cover is expected to vary in phase on seasonal, interannual, and decadal timescales. Slight differences in radiation and precipitation forcing might cause some inter-model spread of sea-ice thickness, snow depth, and nutrient distributions.

While a variety of model configuration, grid size, initial and lateral boundary conditions, and atmospheric forcing are adopted, this intercomparison framework without any arbitrary choices of experimental designs is rather favorable to estimate a potential range of the ice-PP uncertainty.

2.6. Observational Data for Model Validation

In contrast to pelagic phytoplankton, ice-algal properties are not principally measured by satellite remote sensing, and data availability is spotty. In the present study, the simulated ice-PP is compared with available literature values from in situ sampling. For example, the trans-Arctic expedition onboard the U.S. icebreaker Polar Sea created the ice-PP data set in July–August 1994 (Gosselin et al., 1997). The Shelf-Basin Interaction (SBI) campaign provided another cruise opportunity of ice-algal measurements onboard the U.S. icebreaker Healy along the Chukchi and Beaufort shelf slope in May–June 2002 (Gradinger, 2009). These estimates are called as PS94 and HL02, respectively, hereafter. Other data sources mainly based on Leu et al. (2015) are also referred to in the following sections. For unit conversion, the relationship of 1 mmol N = 80 mg C = 1.6 mg Chl is assumed using a C/Chl mass ratio of 50 and a C/N Redfield ratio of 6.625, as in Watanabe et al. (2015) for simplicity, although the observed ice-algal metabolism has variable ratios depending on light and nutrient availability (Vancoppenolle, Meiners, et al., 2013; Niemi & Michel, 2015). Note that a variable C/Chl ratio is adopted only in the UAF models.

The simulated SIC is evaluated by two products of the Special Sensor Microwave/Imager (SSM/I), which are derived from the Bootstrap and NASA Team algorithms, respectively. The Climate Data Record of Passive Microwave Sea Ice Concentration version 3 data set was downloaded from the National Snow and Ice Data Center (NSIDC) website (http://nsidc.org/data/G02202). The SIC below 0.15 is set to zero based on a traditional approach (Parkinson & Cavalieri, 2008). The missing values due to orbital restriction and sensor troubles are excluded from the calculation of spatial and temporal averages.

The simulated snow depth on sea ice is compared with the Arctic Meteorology and Climate Atlas complied by the Environmental Working Group (EWG). This atlas includes Arctic snow depth fields north of 70°N based on field measurements for 1954–1991 (Warren et al., 1999). Gridded monthly climatology data were downloaded from the NSIDC website (https://nsidc.org/data/G01938).

The simulated sea-ice thickness is compared with the Unified Sea Ice Thickness Climate Data Record complied at the University of Washington (Lindsay & Schweiger, 2013). Two submarine-based data sets labeled as "US-Subs-An" and "US-Subs-Dg," respectively (http://psc.apl.uw.edu/sea_ice_cdr/), were downloaded from the NSIDC website (https://nsidc.org/data/G10006). The sea-ice draft for 1980–2009 are chosen and named as "USSUB" for comparison. Since spatial coverage of these data is confined to the central Arctic basins, we added the CryoSat-2 (CS-2) spring (March–April) and fall (October–November) composites in each year of 2010–2016 (Laxon et al., 2013). The pan-Arctic gridded data set was downloaded from the Centre for Polar Observation and Modelling Data Portal (http://www.cpom.ucl.ac.uk/csopr/seaice.html). Since the data period does not cover the model intercomparison target (i.e., 1980–2009), a degree of temporal biases might be present in the assessment.

The simulated nitrate concentration in the ocean surface layer is evaluated using the GLODAPv2 product (Olsen et al., 2016). The "Merged and Adjusted Data Product" (GLODAPv2.2019_Arctic Ocean.csv) was downloaded from the GLODAP website (https://www.glodap.info/). The station data at the depth of 0–2 m for 1980–2009 were chosen. Since the gridded version of the GLODAPv2 package includes numerous missing values in the central Arctic basins, the WOA13 seasonal climatology (Garcia et al., 2013) is included for comparison. The winter (January–March), spring (April–June), summer (July–September), and autumn (October–December) fields were downloaded from the NOAA National Oceanographic Data Center (https://www.nodc.noaa.gov/OC5/woa13/).

3. Pan-Arctic Distribution of Ice-Algal Productivity

The pan-Arctic spatial pattern of annual total ice-PP (i.e., photosynthesis minus respiration of ice algae as introduced in sections 1 and 2.5) averaged for 1980–2009 is commonly characterized by a shelf-basin contrast (Figure 1a). Higher productivity is simulated especially in the Chukchi Sea, the Laptev Sea, and the Canadian Polar Shelf. The ice-PP in the central Arctic Ocean is clearly low. The UAF-G and UAF-R models simulate more ice-PP in the Bering Sea than in the Chukchi Sea. The ice-PP in the UW model is considerably higher than the other models in most Arctic regions.

Here the Entire Arctic region is defined by the southern boundary of 66°N in the Pacific side and 80°N for 90°W–10°E in the Atlantic side (Figure 2). The Bering Sea, the Baffin Bay, and the Nordic seas are excluded for the main analyses. The Arctic Continental Shelf and Central Basin regions are separated by the 1,000 m isobath (Figure 2). The total area of the defined Entire Arctic, Continental Shelf, and Central Basin regions in the five models is 10.12–10.71, 5.90–6.56, and 4.12–4.22 Mkm^2 ($=10^6$ km^2), respectively (Table 3). In this definition, the shelf region is 1.5 times wider than the central basin. The simulated annual total ice-PP in the Entire Arctic region broadly varies from 2.79 ± 0.33 Tg C in the UAF-G model to 21.35 ± 3.87 Tg C in the UW model (Table 3). The simulated range is comparable with previous pan-Arctic estimates of 9–73 Tg C (Legendre et al., 1992), 15.1 Tg C (Deal et al., 2011), and 21.3 Tg C (Jin, Deal, et al., 2012), although our target region and period are smaller and longer, respectively.

Insufficient observational data of annual total ice-PP on longer timescales prevent confident validation of the model outputs. At this stage it is meaningful to understand potential uncertainties quantitatively and assess the relationship with controlling factors based on a multi-model intercomparison as a preliminary step. The ice-PP averaged in a specific region depends on a combination of light intensity and nutrient contents at the sea ice-ocean interface in addition to total ice area for ice-algal habitat. Here, spatial distributions

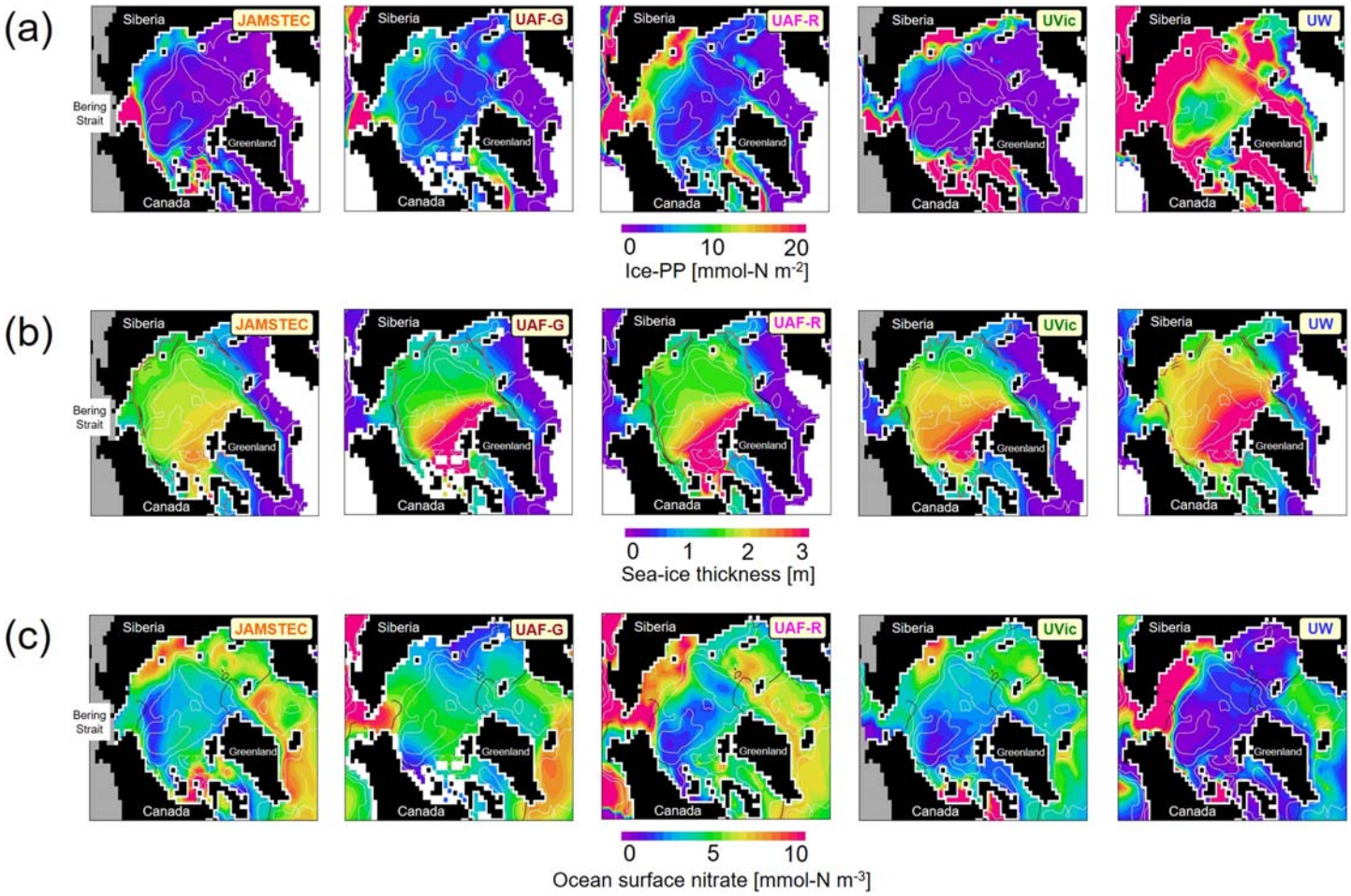

Figure 1. The pan-Arctic spatial distribution of (a) ice-PP (mmol N m^{-2}), (b) sea-ice thickness (m), and (c) nitrate concentration in the ocean surface layer (mmol N m^{-3}) simulated in the JAMSTEC, UAF-G, UAF-R, UVic, and UW models. The annual (a) total and (b–c) mean values averaged for 1980–2009 are shown. The original outputs in each model are remapped to a common polar-stereo coordinate for comparison in this figure. White contours show seafloor depths of 100, 1,000, and 3,000 m, respectively. In (b), sea-ice margin defined by sea-ice concentration of 0.15 in September is overlaid: Red contours correspond to each model result, and black inner (outer) contours denote the SSM/I product derived from the Bootstrap (NASA Team) algorithm. In (c), the WOA13 nitrate concentration of 5 mmol N m^{-3} is overlaid by black contours.

and regional averages of the annual mean sea-ice thickness and nitrate concentration in the ocean surface layer are evaluated.

The sea-ice thickness and edge are similar in the five models (Figure 1b). The UAF-G, UAF-R, UVic, and UW models produce multi-year ice thicker than 3 m north of the Canadian Arctic Archipelago (CAA), whereas thinner ice is simulated in the JAMSTEC model. The validation with submarine and satellite data is addressed in section 4. The sea-ice margin defined using the SIC of 0.15 is similarly located in all five models and the SSM/I products in September (Figure 1b). The location of the simulated sea-ice margin is largely controlled by the atmospheric reanalysis forcing data such as surface air temperature. No sensitivity of sea-ice thickness to the atmospheric forcing or horizontal resolution is seen within this comparison (Figure 1b, Table 3).

The nitrate concentration in the ocean surface layer also shows a shelf-basin contrast (Figure 1c, Table 3). This feature is quite vivid in the UW model, which has fine horizontal resolution in the Chukchi Sea. The minimum concentration is located around the Canada Basin, except in the UAF-G model that produces a ridge-like structure from the East Siberian Sea to the CAA. It is well known that anti-cyclonic wind associated with the Beaufort High accumulates oligotrophic fresher water inside the central Canada Basin

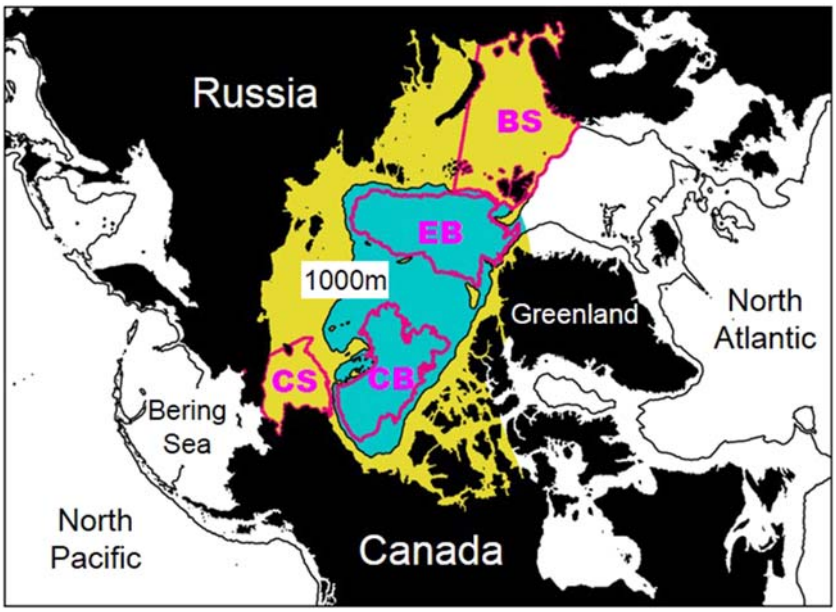

Figure 2. The Arctic Continental Shelf and Central Basin regions defined in section 3 are shown by yellow and blue shades, respectively. The Chukchi Sea (CS), Canada Basin (CB), Eurasian Basin (EB), and Barents Sea (BS) regions defined in section 4 are enclosed by magenta contours, respectively. Black contours denote the seafloor depth of 1,000 m.

(McLaughlin & Carmack, 2010; Proshutinsky et al., 2002). However, as described in section 2.5 and Jin et al. (2018), the Arctic grid size of 18–62 km in the UAF-G model would be insufficient to keep steep isopyncal front along the shelf-basin boundary, in contrast to the UAF-R model. According to the WOA13 annual climatology, nitrate concentrations higher than 5 mmol N m^{-3} are seen in the Chukchi Sea and the Nordic seas (Figure 1c). An obvious discrepancy between the simulated and WOA13 values remains over the Siberian

Table 3
Ice-PP, Sea-Ice Thickness, and Ocean Surface Nitrate Are Integrated (Only For Ice-PP) or Averaged in the Entire Arctic, Continental Shelf, and Central Basin Regions, Respectively

		JAMSTEC	UAF-G	UAF-R	UVic	UW
Area total ice-PP (Tg C)	Entire Arctic	9.03 ± 1.62	2.79 ± 0.33	3.90 ± 0.46	5.15 ± 1.83	21.35 ± 3.87
	Continental Shelf	8.16 ± 1.64	1.84 ± 0.23	3.02 ± 0.39	4.89 ± 1.69	16.55 ± 3.39
	Central Basin	0.88 ± 0.56	0.95 ± 0.15	0.88 ± 0.14	0.26 ± 0.25	4.80 ± 0.86
	Shelf/Basin ratio	9.27	1.94	3.43	18.81	3.45
Area mean ice-PP (mmol N m^{-2})	Entire Arctic	10.54 ± 1.89	3.45 ± 0.41	4.72 ± 0.56	6.26 ± 2.22	25.93 ± 4.70
	Continental Shelf	15.55 ± 3.13	3.90 ± 0.48	6.10 ± 0.78	9.93 ± 3.43	33.52 ± 6.86
	Central Basin	2.63 ± 1.70	2.83 ± 0.44	2.66 ± 0.42	0.80 ± 0.74	14.56 ± 2.61
	Shelf/Basin ratio	5.91	1.38	2.29	12.41	2.30
Sea-ice thickness (m)	Entire Arctic	1.41 ± 0.14	1.62 ± 0.17	1.70 ± 0.21	1.58 ± 0.21	1.95 ± 0.17
	Continental Shelf	1.14 ± 0.14	1.42 ± 0.13	1.56 ± 0.17	1.20 ± 0.18	1.56 ± 0.17
	Central Basin	1.85 ± 0.14	1.91 ± 0.24	1.91 ± 0.27	2.15 ± 0.27	2.53 ± 0.17
	Shelf/Basin ratio	0.62	0.74	0.82	0.56	0.62
Ocean surface nitrate (mmol N m^{-3})	Entire Arctic	4.29 ± 0.50	3.69 ± 0.61	4.53 ± 0.46	3.69 ± 0.13	4.76 ± 1.65
	Continental Shelf	5.06 ± 0.55	3.63 ± 0.30	5.63 ± 0.36	4.57 ± 0.30	7.26 ± 2.73
	Central Basin	3.07 ± 0.62	3.77 ± 1.06	2.88 ± 0.74	2.38 ± 0.23	1.01 ± 0.14
	Shelf/Basin ratio	1.65	0.96	1.95	1.92	7.19
Total area (Mkm^2) (=10^6 km^2)	Entire Arctic	10.71	10.12	10.33	10.28	10.29
	Continental Shelf	6.56	5.90	6.19	6.15	6.17
	Central Basin	4.15	4.22	4.13	4.12	4.12
	Shelf/Basin ratio	1.58	1.40	1.50	1.49	1.50

Note. Annual total ice-PP, annual mean sea-ice thickness, and annual mean ocean surface nitrate averaged for 1980–2009 are listed with standard deviation of interannual variability. Shelf/basin ratio is calculated using each decadal average.

shelves. It is unclear whether this bias is derived from the model performance or the interpolation of sparse sampling data for the WOA13 gridded product. A detailed comparison with the GLODAPv2 station data and the WOA13 seasonal climatology is discussed in section 4.

Annual mean sea-ice thickness and ocean surface nitrate averaged over the Entire Arctic region are both slightly larger in the UW model, but no significant differences appear among the five models (Table 3, Figure 3). With respect to inter-model spreads, relationships of annual ice-PP with sea-ice thickness and ocean surface nitrate are weak. It is expected that higher ice-PP in the shelf region is simulated due to a combination of thinner sea ice and nutrient-rich conditions relative to those in the central basin region (Table 3, Figure 3). The shelf-basin ratio of the area total (area mean) ice-PP widely varies from 1.94 (1.38) in the UAF-G model to 18.81 (12.41) in the UVic model, whereas shelf-basin contrasts of sea-ice thickness and ocean surface nitrate have factors of >0.5 and <2.0, respectively, in the five models (Table 3). This indicates high sensitivity of the simulated ice-PP to differences in annual mean sea-ice thickness and ocean surface nitrate potentially controlling light and nutrient limitation terms in the UVic model. On the other hand, a shelf-basin ratio of the area mean ice-PP is 2.30, which is smaller than that of ocean surface nitrate (7.19) in the UW model in contrast to other models (Table 3: i.e., low sensitivity). Such a situation can occur when the sufficient nitrate remains (or is replenished) on the shelves after spring bloom.

4. Seasonal Transition

Seasonal transitions in the simulated ice-PP and potential key factors averaged for 1980–2009 are analyzed. Light and nutrient limitation factors in the ice-algal photosynthesis term (i.e., (1) in section 2.5) are functions of snow depth, sea-ice thickness, and nitrate conditions at the sea ice-ocean interface. In addition, the ice-PP in each model grid cell depends on the SIC. Therefore, these variables are selected as controlling properties for ice-PP in the present study. It should be noted that light intensity entering the ice-algal habitat is difficult to be validated using in situ data and is not a simple measure of the light limitation factor due to different formulations and parameter values among the five models. The simulated values in each model grid are spatially averaged in the four subregions: Chukchi Sea, Canada Basin, Eurasian Basin, and Barents Sea, respectively (Figure 2). Each subregion has unique hydrographic and biogeochemical characteristics influenced by seafloor depths, Pacific water, Atlantic water, and wind pattern. Hence this method is reasonable to capture geographical contrasts of ice-PP and background environments. The exact definition of these regions is described in the following subsections. The grid numbers in each subregion differ widely among the five models (Table 4), which adopt a variety of horizontal resolution and coordinate systems (see section 2 and Table 1). The spatial distribution inside each subregion is not discussed here for simplicity. Sea-ice properties in open-water grid cells are counted as zero values for calculation of the subregion averages presented here.

4.1. Chukchi Sea

The Chukchi Sea region is defined by 155–180°W, 66°N at the southern boundary, and the seafloor depth of 100 m along the Chukchi shelf break (Figure 2). The total area is 0.47–0.52 Mkm^2 (Table 4). The total numbers of the model grid points vary from 139 in the UAF-G model to 5,854 in the UAF-R model.

The simulated ice-algal spring bloom starts in February–March, immediately after the end of polar night at this latitude (Figure 4a). The simulated daily productivity reaches its peak in April–May. The growth rate and peak values are clearly different among the models. The ice-PP simulated in the UW model is characterized by the highest spring peak of 1.18 mmol N m^{-2} day^{-1} in mid-May and moderate fall bloom in October. The JAMSTEC model also simulates a prominent spring bloom. The peak values in the UAF-G, UAF-R, and UVic models are comparatively small. This range is close to the observational estimates in the northern Chukchi Sea: the PS94 of 47 ± 46 mg C m^{-2} day^{-1} (0.59 ± 0.58 mmol N m^{-2} day^{-1}) in July–August (Gosselin et al., 1997) and the HL02 of 20–30 mg C m^{-2} day^{-1} (0.25–0.38 mmol N m^{-2} day^{-1}) in May–June (Gradinger, 2009). The regional and decadal averages in the five models show negligible ice-PP for July–August (Figure 4a). The ice-algal biomass shows a similar seasonal transition (Figure 4b). However, the highest spring peak of 5.58 mmol N m^{-2} is simulated in the UAF-R model. The peak value in the UW model is 1.05 mmol N m^{-2}, which is close to the UVic model result (0.79 mmol N m^{-2}). For a reference, the PS94 campaign reported the biomass of 9.1 mg C m^{-2} (0.11 mmol N m^{-2}) for the 74–78°N section later in the season (Gosselin et al., 1997).

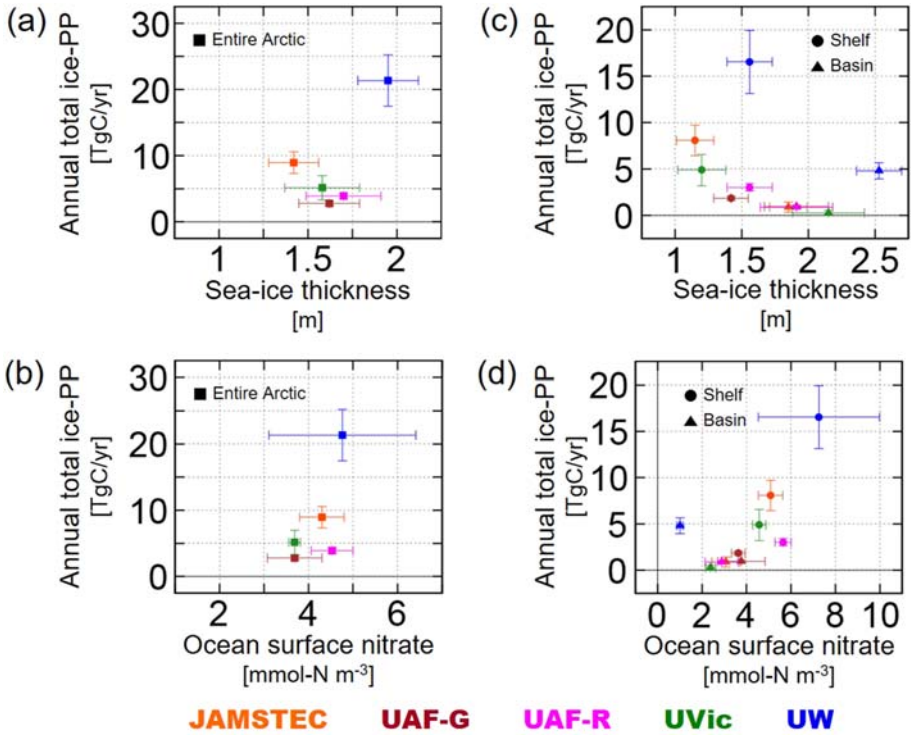

Figure 3. Relationship of annual total ice-PP (mmol N m^{-2}) with annual mean (a) sea-ice thickness (m) and (b) nitrate concentration in the ocean surface layer (mmol N m^{-3}) simulated in the (orange) JAMSTEC, (brown) UAF-G, (magenta) UAF-R, (green) UVic, and (blue) UW models. The decadal mean values for 1980–2009 (a) integrated and (b) averaged in the entire Arctic region are plotted by symbols, and those standard deviation of interannual variability are shown by error bars. Variables in (c–d) are same as those in (a–b) except the (circle symbols) Arctic Continental Shelf and (triangle symbols) Central Basin regions.

The simulated sea-ice concentration averaged in the Chukchi Sea region reproduces well the SSM/I Bootstrap and NASA Team products (Figure 4c). The Chukchi Sea is entirely covered by sea ice from January to April. The sea-ice coverage gradually shrinks after early May and is mostly lost in mid-September. Although the UVic model keeps the minimum concentration to 0.19, the ice-PP is not visible as in the other models for July–August.

The simulated peak of snow depth on sea ice shows a wide range from 0.15 m in the UAF-R model to 0.45 m in the JAMSTEC model (Figure 4d). The peak timing is early May in all the models. The subsequent snow melting for several weeks rapidly enhances light penetration through the underlying sea-ice column. No snow cover is simulated for July–September. The simulated snow depth (except for the JAMSTEC model) is smaller than the EWG monthly climatology (Warren et al., 1999) throughout the year. However, the latter data set is compiled using drift station measurements for 1954–1991 and gridded only north of 70°N (at two points in the Chukchi Sea region). Thus, temporal and spatial biases are possible.

Table 4
Total Areas (Mkm^2 [$=10^6$ km^2]) in the Chukchi Sea, Canada Basin, Eurasian Basin, and Barents Sea Regions

	JAMSTEC		UAF-G		UAF-R		UVic		UW	
Chukchi Sea	0.52	(681)	0.47	(139)	0.49	(5,854)	0.50	(2,845)	0.50	(5,583)
Canada Basin	0.88	(1,157)	0.90	(432)	0.91	(10,729)	0.87	(5,276)	0.95	(3,759)
Eurasian Basin	1.14	(1,477)	1.15	(798)	1.20	(14,003)	1.14	(5,958)	1.23	(804)
Barents Sea	1.65	(2,203)	1.55	(784)	1.57	(18,918)	1.62	(8,011)	1.52	(424)

Note. Total numbers of the model grid points in each subregion are shown in parentheses.

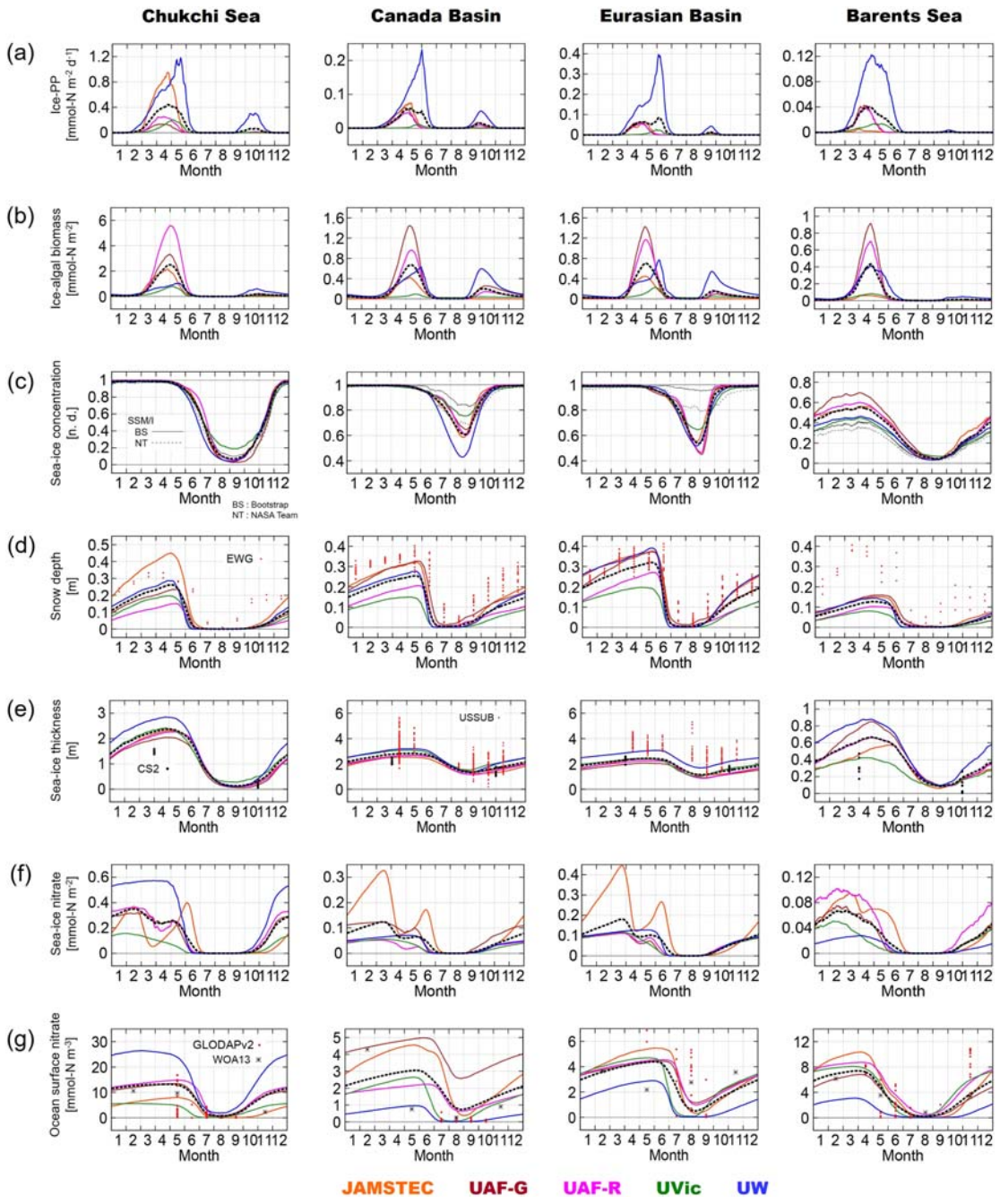

Figure 4. Seasonal transitions in (a) ice-PP (mmol N m^{-2} day^{-1}), (b) ice-algal biomass (mmol N m^{-2}), (c) sea-ice concentration (non-dimensional (n. d.)), (d) snow depth (m), (e) sea-ice thickness (m), (f) nitrate content in the sea-ice column (mmol N m^{-2}), and (g) nitrate concentration in the ocean surface layer (mmol N m^{-3}) simulated in the (orange) JAMSTEC, (brown) UAF-G, (magenta) UAF-R, (green) UVic, and (blue) UW models. Daily mean values averaged for 1980–2009 and in the four subregions are shown. The multi-model averages are plotted by black dashed lines. A thin solid (dashed) line in (c) shows the SSM/I product derived from the bootstrap (NASA Team) algorithm. In (d), red dots show the EWG monthly climatology. In (e), the USSUB data are plotted by red dots. Black dots show the CryoSat-2 March–April and October–November averages in each year of 2010–2016. In (g), the GLODAPv2 data are plotted by red dots. Black symbols show the WOA13 seasonal climatology.

The simulated spring sea ice is thicker than the CS-2 product (Figure 4e). The peak thickness ranges from 2.05 m in the UAF-G model to 2.85 m in the UW model. Since the average period of 1980–2009 in the models does not overlap with 2010–2016 in the CS-2 operation, the trend in sea-ice decline could account for this discrepancy. Seasonal transition in sea-ice thickness is slow relative to the snow depth. Sea-ice melting

continues for May–September. The simulated thickness in the fall season is comparable with the CS-2. The ranking of sea-ice thickness among the models is different from that of snow depth, partly because heavy snow cover sometimes restricts thermal sea-ice growth. The summer reduction in sea-ice thickness is the largest in the UW model. In general, the higher melting rate promotes release of ice algae from the skeletal layer.

The nitrate concentration vertically integrated in the sea-ice column shows two types of seasonal transition (Figure 4f). After nutrient uptake of ice algae at the initial stage of spring bloom, the nitrate content recovers around April in the JAMSTEC, UAF-G, and UAF-R models. The remineralization process from organic materials accounts for the second peak in these models (not shown). This double spring peak is not seen in the UVic and UW models. The annual maximum content ranges from 0.16 mmol N m^{-2} in the UVic model to 0.57 mmol N m^{-2} in the UW model. The sea-ice nitrate is entirely depleted primarily by both ice-algal uptake and meltwater flushing into the underlying ocean layer for July–September in the five models.

The annual maximum nitrate concentration in the ocean surface layer also shows a wide range from 5.57 mmol N m^{-3} in the UVic model to 26.48 mmol N m^{-3} in the UW model (Figure 4g). Whereas the multi-model average is slightly higher than the WOA13 seasonal climatology except the summer value, most model values are within the GLODAPv2 station data in May. It is suggested that the higher ocean surface nitrate and sea-ice freezing rate contribute to more accumulation of sea-ice nitrate during winter (Figure 4f) and subsequent massive spring ice-PP (Figure 4a) in the UW model relative to the other models.

4.2. Canada Basin

The Canada Basin region is defined by the seafloor depth of 3,000 m within 100–180°W and 70–85°N (Figure 2). In the UW model, the water depth of 3,000 m is located between the vertical layer boundaries of 2,825 and 3,358 m, so 2,825 m is chosen to calculate the area average. This choice causes no crucial bias as shown in the total area of 0.87–0.95 Mkm^2 (Table 4).

The simulated ice-algal bloom starts in March and reaches an ice-PP peak of 0.01–0.23 mmol N m^{-2} day^{-1} in April–June (Figure 4a). The ice-PP is the most prominent in the UW model like in the Chukchi Sea. On the other hand, the ice-algal biomass peak ranges from 0.09 mmol N m^{-2} in the UVic model to 1.44 mmol N m^{-2} in the UAF-G model (Figure 4b). Compared with the Chukchi Sea averages, the bloom timing is somewhat later, and the magnitude is substantially lower in the Canada Basin. The fall bloom is visible in the UAF-G and UAF-R models in addition to the UW model. To the best of our knowledge, no validation data of the ice-PP are available for the Canada Basin region defined in the present study (The PS94 transected west of the Chukchi Borderland; Gosselin et al., 1997).

Most areas of the Canada Basin are usually covered by sea ice throughout the year (Figure 4c). The multi-model average sea-ice concentration exceeds 0.60 even in September. Whereas the summertime value is somewhat low relative to the SSM/I products, sea-ice opening and closing periods are almost the same. The UVic (UW) model shows a relatively large (small) concentration for July–September. The snow depth has a wide range of its peak from 0.15 m in the UVic model to 0.33 m in the UAF-G model (Figure 4d), which is smaller than the EWG monthly climatology (Warren et al., 1999). The peak timing in late May is a few weeks later compared to the Chukchi Sea average. The simulated sea-ice thickness is slightly larger than the CS-2 product (Figure 4e) probably because of the same reason for the Chukchi Sea (see section 4.1). Actually, the simulated values are within the range of the USSUB data.

The sea-ice nitrate shows a similar seasonal transition with lower peak values relative to the Chukchi Sea average (Figure 4f). The ocean surface nitrate is not entirely depleted throughout the year in the JAMSTEC, UAF-G, and UAF-R models (Figure 4g). This feature is inconsistent with the GLODAPv2 station data, whose values are near zero. The multi-model average is larger than the WOA13 seasonal climatology except the winter value. The annual peak values differ widely among the models. A possible factor for this discrepancy is derived from the model's ability to represent shelf-basin exchange. Higher nitrate concentration is simulated by the UAF-G and JAMSTEC models, which have horizontal grid sizes above 20 km in the western Arctic. A number of previous studies have indicated that the shelf-basin exchange of hydrographic and biogeochemical properties across the Chukchi and Beaufort shelf break was induced by mesoscale eddies (e.g., Pickart, 2004; Spall et al., 2008; Watanabe et al., 2014). In addition, a substantial amount of shelf-origin water is transported from the Barrow Canyon mouth toward the Chukchi Borderland by a narrow boundary

current named the Chukchi Slope Current (Corlett & Pickart, 2017; Spall et al., 2018; Watanabe et al., 2017). Thus, in the Canada Basin, crucial nitrate biases are sometimes produced by the coarser-resolution models which hardly resolve mesoscale eddies and boundary currents.

4.3. Eurasian Basin

The Eurasian Basin region is defined by the seafloor depth of 3,000 m (again, 2,825 m in the UW model) within 80°W–150°E (the Atlantic side) and 78–90°N plus a small part of the western Arctic around the North Pole (Figure 2). The total area is 1.14–1.23 Mkm^2 (Table 4).

Seasonal transition in the ice-PP is similar to the Canada Basin average, except its spring peak of 0.39 mmol N m^{-2} day^{-1} which is two times larger in the UW model (Figure 4a). The amplitudes in the other four models are below 0.07 mmol N m^{-2} day^{-1}. For a reference, the PS94 of 5 ± 1 mg C m^{-2} day^{-1} (0.06 ± 0.01 mmol N m^{-2} day^{-1}) was estimated at two stations within 84–86°N and 35–38°E northeast of Fram Strait (Gosselin et al., 1997). Recent field sampling in late summer 2011/2012 recorded a wide range of the ice-PP up to 9.2 mg C m^{-2} day^{-1} (0.12 mmol N m^{-2} day^{-1}) for pack ice and 40 mg C m^{-2} day^{-1} (0.50 mmol N m^{-2} day^{-1}) for sub-ice aggregates, respectively, in the Eurasian Basin (Assmy et al., 2013; Fernández-Méndez et al., 2014). The ice-algal biomass peak from 0.23 mmol N m^{-2} in the UVic model to 1.43 mmol N m^{-2} in the UAF-G model (Figure 4b) is slightly lower than 1.23–4 mg Chl m^{-2} (0.77–2.5 mmol N m^{-2}) measured during a ship-based campaign in summer 2012 (Castellani et al., 2017).

The sea-ice cover during the melting season is underestimated by all the models (Figure 4c). Since the SSM/I orbit could not track a part of the Eurasian Basin region around the North Pole (>84.5°N until June 1987, >87.2°N for July 1987–December 2007, >89.2°N after January 2008), the missing zone is excluded from the average area of the SSM/I-derived SIC. However, the SIC around the North Pole is mostly higher than that at lower latitudes. This treatment does not account for the simulated SIC bias. The snow depth peaks at 0.20 m in the UVic model to 0.39 m in the UW model, which is slightly larger than in the Canada Basin (Figure 4d). The timing and duration of snow melting and accumulation are similar among the five models and the EWG monthly climatology. The multi-model average of sea-ice thickness is consistent with the CS-2 spring and fall data (Figure 4e). If sea-ice thinning occurred as in the western Arctic, the thickness in the Eurasian Basin would be underestimated, as suggested by comparison with the USSUB data.

The nitrate contents show similar seasonal cycles to the Canada Basin averages (Figures 4e–4f). The simulated phase in the ocean surface nitrate seems to be delayed for a couple of months relative to the WOA13 seasonal climatology. The annual minimum season is summer (July–September) in the models and spring (April–June) in the WOA13. On the other hand, the simulated nitrate concentration in August is clearly lower than the GLODAPv2 station data. It is now difficult to identify a primary factor for the nitrate biases.

4.4. Barents Sea

The Barents Sea region is defined by 10–55°E and the seafloor depth of 1,000 m facing the Eurasian Basin (Figure 2). In the UW model, the water depth of 1,000 m is located between the vertical layer boundaries of 862 and 1,073 m, so 1,073 m is alternatively chosen to calculate the area average. The total area is 1.52–1.65 Mkm^2, which is the largest among the four subregions (Table 4). Whereas sea ice does not extend over the entire Barents Sea region all year round as shown in the SIC seasonal transition below, any alternative definition would be arbitrary. The grid point number broadly ranges from 424 in the UW model to 18,918 in the UAF-R model.

A spring peak in the ice-PP varies from 0.01 mmol N m^{-2} day^{-1} in the JAMSTEC model to 0.12 mmol N m^{-2} day^{-1} in the UW model (Figure 4a). The ice-algal biomass peak ranges from 0.06 mmol N m^{-2} in the JAMSTEC model to 0.91 mmol N m^{-2} in the UAF-G model (Figure 4b). These values are the lowest among the four subregions. The fall bloom signal is also quite weak unlike that in the other subregions. The spring SIC peak ranging from 0.45 in the UVic model to 0.70 in the UAF-G model is comparatively larger than the SSM/I products (Figure 4c). The rapid snow melting similarly appears in June (Figure 4d). The sea ice is mostly thicker than the CS-2 (Figure 4e). It is known that the warm Atlantic water inflow from the Nordic seas (so-called "the Barents Sea Branch Water") forms the marginal ice zone in the Barents Sea (Årthun et al., 2012). The simulated sea-ice bias might originate from insufficient lateral heat flux associated with the Atlantic water transport.

It should be noted that the average area includes open-water grid cells in the Barents Sea region. If the model properties are averaged only over grid points with daily mean SIC >0.15, ice-PP of 0.01–0.24 mmol N m^{-2} day^{-1}, ice-algal biomass of 0.10–1.24 mmol N m^{-2}, snow depth of 0.17–0.32 m, and sea-ice thickness of 0.94–1.95 m are obtained as peak values (not shown). Even then, these averages of the ice-PP, ice-algal biomass, and sea-ice thickness are still smaller than the Chukchi Sea averages (Figures 4a and 4d). In the northern Barents Sea, the ice-PP of 4.9–55 mg C m^{-2} d^{-1} (0.06–0.69 mmol N m^{-2} day^{-1}) and the pigment content of 18.5 ± 8.9 mg Chl m^{-2} (11.56 ± 5.56 mmol N m^{-2}) were measured in May 2004 (McMinn & Hegseth, 2007). Sampling in July 2003/2004 suggested ice-algal biomass of 9–620 mg C m^{-2} (0.11–7.75 mmol N m^{-2}) (Tamelander et al., 2009).

The sea-ice (ocean surface) nitrate content has a peak value of 0.03–0.10 mmol N m^{-2} (3.09–10.36 mmol N m^{-3}) in the entire Barents Sea region (Figures 4e–4f) and 0.06–0.16 mmol N m^{-2} (1.38–9.59 mmol N m^{-3}) for the sea-ice grid cells. The nitrate decline during the melting season is similar to the GLODAPv2 station data, and nitrate availability at the sea ice-ocean interface is also lower than for the Chukchi Sea average.

4.5. Key Findings

The simulated spring ice-algal bloom starts immediately after the end of polar night in each subregion. The peak values of the ice-PP are broadly different among the four subregions and among the five models, respectively. The highest peak in the Chukchi Sea and the lowest one in the Barents Sea are simulated. The ice-PP in the central basins is moderate. In addition, the UW model produces the highest ice-PP in all four subregions. A fall bloom is evident in the UAF-G, UAF-R, and UW models.

The simulated sea-ice, snow, and ocean properties related to ice algae qualitatively reproduce seasonal transitions with large variability in annual peak values in the four subregions. Whereas the SIC in the Chukchi Sea reproduces the satellite observations, negative (positive) SIC biases appear in the Canada and Eurasian basins (Barents Sea). The snow depth is smaller than the EWG monthly climatology potentially due to a gap in averaging periods. The sea-ice thickness generally falls in between the USSUB and CS2 data in the central basins. The nitrate value widely varies among the five models and among the GLODAPv2 station data, respectively. The higher-resolution models tend to retain the bowl-shaped structure of the nutricline in the Beaufort Gyre region (Jin et al., 2018). A distinct inter-model spread appears in the simulated snow depth even when the common atmospheric forcing data set is used (Table 1: CFSR for the JAMSTEC and UW experiments, CORE II for the UAF-G and UAF-R experiments). A simulated nitrate spread among the five models is not primarily derived from choice of the initial fields (Table 1: WOA13, WOA05, and GLODAPv2) or the model domain. Further discussions on model biases of these controlling factors are out of the scope of this study.

5. Interannual and Decadal Variability

The decadal time series for 1980–2009 of the annual total ice-PP, minimum SIC, and maxima of snow depth, sea-ice thickness, sea-ice nitrate content, and ocean surface nitrate concentration averaged for each subregion are shown in Figure 5. The annual minimum SIC recorded in every September is a key index of sea-ice decline on the interannual and decadal timescales. The annual maxima of snow depth, sea-ice thickness, and nitrates represent preconditions for the ice-algal bloom in spring. Note that some simulated values are multiplied by a factor for better comparison of interannual variability in Figure 5 (see details in figure caption). The decadal trends for each model and property are listed in Table 5. The relationship of the annual total ice-PP with the annual peak values selected above (i.e., the minimum for SIC and the maximum for other variables) in the four subregions is also investigated using scatter plots (Figure 6) with respect to both interannual and inter-model variability. The Pearson correlation coefficients (r) of interannual variability in each model are listed in Table 6.

5.1. Chukchi Sea

The multi-model average of the annual total ice-PP is the highest and slightly increasing for 1980–2009 in the Chukchi Sea (Table 5, Figure 5a). However, this ensemble mean reflects two positive trends (the UAF-G and UVic models) and three negative trends (the JAMSTEC, UAF-R, and UW models): None of them are significant (95% level) at least for the 30 years evaluated (Table 5). Overall, the ice-PP time series are characterized by large interannual variability producing substantial standard deviations (Figure 5a).

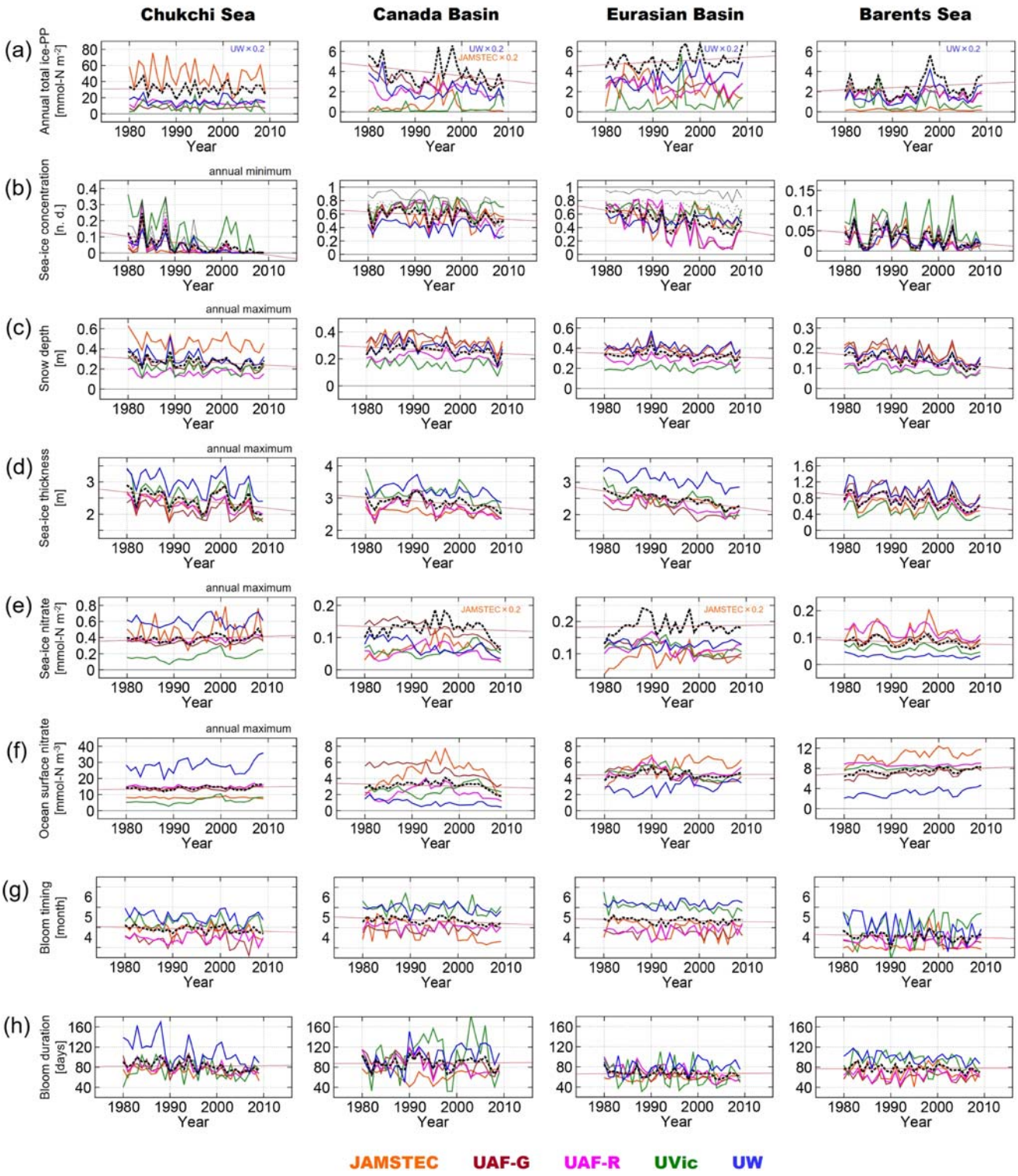

Figure 5. Interannual time series of (a) ice-PP (mmol N m^{-2}), (b) sea-ice concentration (n. d.), (c) snow depth (m), (d) sea-ice thickness (m), (e) nitrate content in the sea-ice column (mmol N m^{-2}), (f) nitrate concentration in the ocean surface layer (mmol N m^{-3}), (g) bloom timing (month), and (h) bloom duration (days) simulated in the (orange) JAMSTEC, (brown) UAF-G, (magenta) UAF-R, (green) UVic, and (blue) UW models. The annual (a) total, (b) minimum, and (c–f) maximum averaged in the four subregions are shown for 1980–2009. The multi-model averages and those decadal trends are plotted by black dashed and red lines, respectively. Decadal trends in each model are listed in Table 5. For better comparison of interannual variability, the UW values are multiplied by 0.2 in (a). Similarly, the JAMSTEC values are multiplied by 0.2 in the Canada Basin in (a) and the Canada and Eurasian Basins in (e). The original ranges are seen in Figures 6–8. A thin solid (dashed) line in (b) shows the SSM/I product derived from the bootstrap (NASA Team) algorithm.

Table 5
Decadal Trend in Annual Total Ice-PP, Annual Peak Values of Major Properties, Bloom Timing, and Bloom Duration in the Four Subregions

			Multi-model average	JAMSTEC	UAF-G	UAF-R	Uvic	UW
Chukchi Sea	Annual total ice-PP	(mmol Nm^{-2})	1.51 ± 1.48	−4.47 ± 3.21	0.13 ± 0.40	−0.27 ± 0.59	0.24 ± 1.28	−1.76 ± 4.79
	Sea-ice concentration	(%)	−3.90 ± 0.93	−1.86 ± 0.81	−2.23 ± 0.94	−4.08 ± 1.27	−8.23 ± 1.79	−3.08 ± 0.65
	Snow depth	(cm)	−2.29 ± 0.98	−2.91 ± 1.45	−2.42 ± 0.89	−0.53 ± 0.68	−1.66 ± 1.22	−3.91 ± 1.39
	Sea-ice thickness	(cm)	−16.33 ± 5.42	−10.79 ± 6.21	−13.11± 4.53	−14.11 ± 4.27	−25.40 ± 7.54	−18.22 ± 6.34
	Sea-ice nitrate	(μmol N m^{-2})	16.90 ± 8.68	20.78 ± 30.27	4.05 ± 6.16	16.37 ± 5.56	31.94 ± 9.93	11.33 ± 14.23
	Ocean surface nitrate	(mmol N m^{-3})	0.49 ± 0.22	−0.02 ± 0.09	0.02 ± 0.21	0.22 ± 0.19	1.11 ± 0.31	1.15 ± 0.81
	Bloom timing	(day)	−2.02 ± 0.93	−3.74 ± 1.64	−2.23 ± 2.17	0.57 ± 1.66	−1.60 ± 1.96	−3.09 ± 1.86
	Bloom duration	(days)	−6.81 ± 1.76	−3.44 ± 1.70	−5.46 ± 2.42	−6.12 ± 2.25	−1.95 ± 4.00	−17.07 ± 4.61
Canada Basin	Annual total ice-PP	(mmol N m^{-2})	−0.49 ± 0.24	−0.05 ± 0.84	−0.30 ± 0.13	−0.10 ± 0.13	0.23 ± 0.12	−2.22 ± 0.85
	Sea-ice concentration	(%)	−3.78 ± 1.97	−1.40 ± 3.17	−6.14 ± 2.41	−8.56 ± 3.13	1.09 ± 2.20	−3.90 ± 1.76
	Snow depth	(cm)	−1.62 ± 0.72	−1.65 ± 1.08	−2.91 ± 0.87	−0.83 ± 0.68	−1.12 ± 0.79	−1.61 ± 1.06
	Sea-ice thickness	(cm)	−10.90 ± 3.17	−5.22 ± 1.84	−9.41 ± 5.13	−12.51 ± 4.87	−16.28 ± 4.83	−11.09 ± 3.83
	Sea-ice nitrate	(μmol N m^{-2})	−2.92 ± 5.84	30.05 ± 24.49	−27.68 ± 2.85	−2.87 ± 4.29	5.38 ± 3.10	−19.46 ± 3.24
	Ocean surface nitrate	(mmol N m^{-3})	−0.14 ± 0.11	0.38 ± 0.32	−0.91 ± 0.09	−0.05 ± 0.17	0.20 ± 0.12	−0.31 ± 0.06
	Bloom timing	(day)	−2.80 ± 1.02	−9.67 ± 2.95	1.32 ± 1.24	−1.29 ± 1.19	−2.37 ± 1.94	−2.00 ± 1.39
	Bloom duration	(days)	−0.87 ± 2.53	−0.00 ± 2.23	−10.17 ± 3.09	−9.26 ± 3.20	3.47 ± 8.52	11.59 ± 4.43
Eurasian Basin	Annual total ice-PP	(mmol N m^{-2})	0.24 ± 0.16	−0.50 ± 0.25	−0.30 ± 0.12	−0.28 ± 0.13	0.19 ± 0.23	2.11 ± 0.76
	Sea-ice concentration	(%)	−10.57 ± 2.00	−0.76 ± 3.00	−22.26± 3.90	−21.74 ± 4.15	−7.64 ± 1.94	−0.48 ± 1.59
	Snow depth	(cm)	−1.39 ± 0.72	−0.35 ± 1.03	−3.97 ± 0.82	−1.90 ± 0.74	0.20 ± 0.70	−0.91 ± 1.09
	Sea-ice thickness	(cm)	−17.76 ± 1.92	−10.79 ± 2.23	−15.23± 3.34	−19.11 ± 2.83	−25.38 ± 4.27	−18.32 ± 3.18
	Sea-ice nitrate	(μmol N m^{-2})	1.69 ± 5.62	45.14 ± 23.97	−20.15± 2.69	−5.09 ± 4.43	−11.17 ± 3.49	−0.00 ± 2.42
	Ocean surface nitrate	(mmol N m^{-3})	−0.02 ± 0.09	0.69 ± 0.19	−0.70 ± 0.10	−0.08 ± 0.17	−0.42 ± 0.13	0.43 ± 0.12
	Bloom timing	(day)	−1.16 ± 0.84	−3.41 ± 2.58	−0.75 ± 1.51	2.85 ± 1.53	−4.63 ± 1.46	0.13 ± 1.19
	Bloom duration	(days)	−3.73 ± 1.44	1.32 ± 1.19	−8.17 ± 1.61	−11.06 ± 2.16	−5.35 ± 5.35	4.61 ± 3.01
Barents Sea	Annual total ice-PP	(mmol N m^{-2})	0.21 ± 0.22	−0.00 ± 0.02	−0.08 ± 0.12	−0.06 ± 0.09	−0.25 ± 0.17	1.44 ± 0.84
	Sea-ice concentration	(%)	−0.94 ± 0.44	−0.72 ± 0.52	−1.20 ± 0.44	−1.11 ± 0.42	−0.96 ± 0.87	−0.69 ± 0.41
	Snow depth	(cm)	−1.97 ± 0.48	−2.10 ± 0.66	−2.99 ± 0.80	−1.43 ± 0.48	−1.08 ± 0.33	−2.24 ± 0.47
	Sea-ice thickness	(cm)	−10.09 ± 3.04	−7.34 ± 3.17	−12.52 ± 3.83	−10.93 ± 2.63	−7.37 ± 2.93	−12.30 ± 3.84
	Sea-ice nitrate	(μmol N m^{-2})	−6.25 ± 3.10	−4.35 ± 7.64	−1.39 ± 2.34	−14.70 ± 4.22	−7.46 ± 2.33	−3.27 ± 1.22
	Ocean surface nitrate	(mmol N m^{-3})	0.39 ± 0.09	0.89 ± 0.19	0.61 ± 0.11	−0.10 ± 0.05	−0.02 ± 0.07	0.57 ± 0.11
	Bloom timing	(day)	−1.44 ± 1.36	1.69 ± 2.46	−3.11 ± 1.36	−1.25 ± 1.70	6.08 ± 4.62	−10.62 ± 3.23
	Bloom duration	(days)	−2.42 ± 1.45	−2.95 ± 3.10	0.25 ± 1.98	1.07 ± 2.05	−5.30 ± 3.37	−5.20 ± 1.98

Note. Error bar indicates asymptotic standard deviation. Red (blue) color means a positive (negative) trend above the 95% significant level. Time series of each property are shown in Figure 5.

The annual minimum of sea-ice area has gradually shrunk over the three decades (Table 5, Figure 5b). After the mid-1990s, sea ice entirely disappears in most years so that the minimum SIC has little interannual variability. An exception is the UVic model, which retains a certain amount of sea ice within the Chukchi Sea even after 2000. The annual maxima of snow depth and sea-ice thickness also show the negative trends (Table 5, Figures 5c–5d). The interannual variability in snow depth and sea-ice thickness are almost in phase among the experiments.

The annual maxima of sea-ice nitrate show statistically significant positive trends in the UAF-R and UVic models) (Table 5, Figures 5e–5f). The ocean surface nitrate is also increasing in the multi-model average and in the UVic model. The suggested contributors to elevating nitrate concentration at the ocean surface in the Chukchi Sea are (1) enhanced vertical mixing derived from sea-ice fragmentation and (2) increased lateral influx from the North Pacific through the Bering Strait. As stated above, nitrate restoring at the Bering Strait in the JAMSTEC model dampens the interannual and decadal variability in the western Arctic. The visible interannual fluctuation of sea-ice nitrate in the JAMSTEC model depends on the sea-ice freezing rate in each year rather than the ocean surface nitrate concentration.

A couple of features emerge from the scatter plots (Figure 6). The first feature is that the annual total ice-PP is linearly related to the annual peak biomass of ice algae in all the models (Figure 6a). The correlation coefficient ranges 0.43–0.88 (Table 6). However, its slope is clearly different among the five models. For example, the UW (UAF-R) model produces an annual total ice-PP of 37–132 (8–19) mmol N m^{-2} with an annual peak

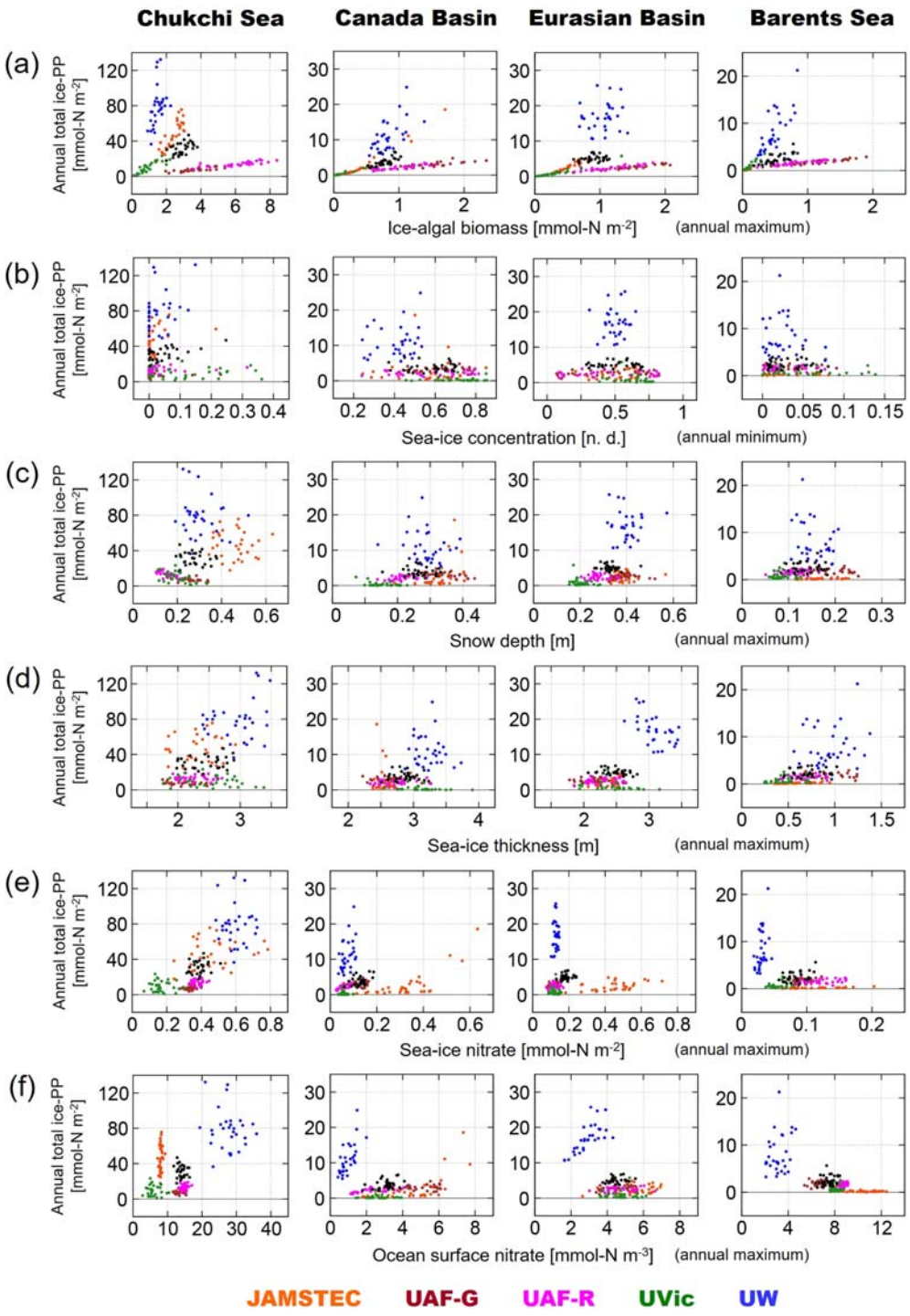

Figure 6. Relationship of annual total ice-PP (mmol N m^{-2}) with (a) ice-algal biomass (mmol N m^{-2}), (b) sea-ice concentration (n. d.), (c) snow depth (m), (d) sea-ice thickness (m), (e) nitrate content in the sea-ice column (mmol N m^{-2}), and (f) nitrate concentration in the ocean surface layer (mmol N m^{-3}) simulated in the (orange) JAMSTEC, (brown) UAF-G, (magenta) UAF-R, (green) UVic, and (blue) UW models. The annual (b) minimum and (a, c–f) maximum averaged in the four subregions are shown for 1980–2009. The multi-model averages are plotted by black dots. Correlation coefficients of two properties in each model are listed in Table 6.

biomass of 0.92–2.25 (3.58–8.40) mmol N m^{-2}. The slope in the UW model is 18 times larger than the UAF-R model. We attribute the higher ratio to (1) a higher growth rate of ice algae per unit biomass and/or (2) larger sink terms such as mortality and sea-ice meltwater flushing (see section 3). The growth rate in the five

Table 6
Correlation Coefficient of Annual Total Ice-PP With Annual Peak Values of Major Properties in the Four Subregions

		Multi-model average	JAMSTEC	UAF-G	UAF-R	UVic	UW
Chukchi Sea	Ice-algal biomass	0.55	0.85	0.75	0.82	0.88	0.43
	Sea-ice concentration	0.56	0.35	0.01	0.14	0.06	0.33
	Snow depth	−0.14	−0.08	−0.40	−0.63	−0.56	−0.16
	Sea-ice thickness	0.21	0.09	−0.36	0.13	0.19	0.24
	Sea-ice nitrate	0.20	0.25	0.28	0.19	0.04	−0.03
	Ocean surface nitrate	−0.10	0.26	0.20	0.24	−0.02	−0.15
Canada Basin	Ice-algal biomass	0.66	0.97	0.75	0.89	0.98	0.60
	Sea-ice concentration	0.04	−0.11	0.16	0.25	0.10	0.15
	Snow depth	−0.02	0.38	−0.18	0.38	−0.48	−0.18
	Sea-ice thickness	−0.01	−0.19	−0.13	0.32	−0.26	−0.10
	Sea-ice nitrate	0.39	0.76	0.19	0.72	−0.06	0.47
	Ocean surface nitrate	0.34	0.62	0.14	0.68	−0.01	0.69
Eurasian Basin	Ice-algal biomass	0.24	0.95	0.92	0.89	0.98	0.16
	Sea-ice concentration	−0.00	0.15	0.25	0.21	−0.17	0.08
	Snow depth	−0.10	0.12	0.06	−0.10	−0.30	0.00
	Sea-ice thickness	−0.28	0.49	0.10	0.25	−0.28	−0.55
	Sea-ice nitrate	0.13	0.48	0.44	0.22	0.02	0.15
	Ocean surface nitrate	0.25	0.34	0.43	0.19	0.03	0.72
Barents Sea	Ice-algal biomass	0.75	0.95	0.93	0.90	0.96	0.78
	Sea-ice concentration	0.02	0.27	−0.17	0.05	0.02	−0.09
	Snow depth	0.09	0.54	0.09	0.26	0.08	−0.28
	Sea-ice thickness	0.21	0.69	0.12	0.25	0.36	0.15
	Sea-ice nitrate	0.44	0.88	0.29	0.30	0.40	0.41
	Ocean surface nitrate	0.23	−0.05	−0.08	0.40	0.13	0.27

Note. Red (blue) color means positive (negative) correlation above the 95% significant level. Yearly values are plotted in Figure 6.

models is determined by photosynthesis parameter values, light, and nutrient availability. The UW model chooses 4.0 day^{-1} as a maximum growth rate of ice algae (V_{maxi}), which is much larger than 1.2 day^{-1} in the JAMSTEC model, 1.44 day^{-1} in the UAF-G and UAF-R models, and 0.85 day^{-1} in the UVic model (section 2.5). Additional experiments performed using the JAMSTEC model support the high sensitivity of the ice-PP to V_{maxi} (not shown).

The second feature is that heavy snow cover is a significant limiting factor for the annual total ice-PP in the UAF-G, UAF-R, and UVic models (Figure 6c). The correlation coefficients in these models are –0.40, –0.63, and –0.56, respectively (Table 6). On the other hand, no correlation between the two properties is seen in the JAMSTEC and UW models. The light availability in the skeletal layer depends on both snow depth and sea-ice thickness. In the case that quite thin ice is caused by thick snow due to its blanket effect during winter freezing, the linkage between the spring snow depth and light intensity at the sea-ice bottom after snow melt completion should be weak.

The third feature is that no significant correlation between the annual total ice-PP and the annual minimum SIC arises in any models (r = 0.01–0.35, Table 6, Figure 6b) for two potential reasons. First, the minimum SIC in the Chukchi Sea has little interannual variability, because sea ice entirely disappears in most years. Second, the mid-summer weather conditions modulate the sea-ice extent after the ice-algal bloom, for example, via wind-driven sea-ice retreat.

5.2. Canada Basin

The simulated annual total ice-PP in the Canada Basin also shows different decadal variability for 1980–2009 among the five models (Figure 5a). The multi-model average shows a negative trend of –0.49 ± 0.24 mmol N m^{-2} per decade (Table 5). The time series in the UW model shows high values in the early 1980s and a subsequent rapid decline (Figure 5a), which results in a significant negative trend of –2.22 ± 0.85 mmol N m^{-2} per decade (Table 5). Whereas the UAF-G model also has a significant negative trend of –0.30 ± 0.13 mmol N

m^{-2} per decade, a small positive trend of 0.23 ± 0.12 mmol N m^{-2} per decade is simulated in the UVic model. The JAMSTEC model produces a distinct peak in the mid-1990s, which is not seen in any of the other models (Figure 5a). The decadal trends in the JAMSTEC and UAF-R models are negligible (Table 5).

The annual peaks of sea-ice area, snow depth, and sea-ice thickness show declining trends (Table 5, Figures 5b–5d). The minimum SIC still has remarkable interannual variability until the 2000s. The sea-ice and ocean surface nitrate contents in the UAF-G and UW models show significant negative trends (Table 5, Figures 5e–5f). An important factor for the nitrate decline at the sea ice-ocean interface of the Canada Basin is the dilution effect due to sea-ice meltwater (Yamamoto-Kawai et al., 2011). However, the highest concentration in the ocean surface layer is simulated for the mid-1990s in the JAMSTEC and UAF-R models and for the early 2000s in the UVic model. Correspondingly, the multi-model average has its peaks in the 1990s. Previous studies have suggested that hydrographic and biogeochemical conditions in the Beaufort Gyre region were controlled by the wind-driven Ekman transport for seasonal to decadal timescales (Proshutinsky et al., 2009). It has been shown that the nutricline in the central basin was shoaling (deepening) under a cyclonic wind regime in the early 1990s (an anti-cyclonic regime after the mid-1990s) (Proshutinsky et al., 2002; McLaughlin & Carmack, 2010; Nishino et al., 2011). This balance of ice melt and wind impacts is expected to characterize the decadal variability in ocean surface nitrate contents, whereas the lateral/vertical transport in the water column is not analyzed in the present study.

As in the Chukchi Sea, the annual total ice-PP is linearly related to the annual peak biomass in each model (Figure 6a). Their correlation coefficient is statistically significant in all models (r = 0.60–0.98, Table 6). The higher ratio in the UW model is not explained by the simulated nitrate content, which is lower than the multi-model average. The higher growth rate is achieved plausibly by the higher photosynthesis parameter value (V_{maxi} = 4.0 d^{-1}). The heavy snow cover in spring limits the annual total ice-PP strongly in the UVic model (r = –0.48, Table 6) and weakly in the UAF-G and UW models (r = –0.18, Table 6). On the other hand, higher ice-PP is simulated under heavy snow in the JAMSTEC and UAF-R models (r = 0.38, Table 6, Figure 6 c). The correlation with sea-ice thickness is low in all five models ($|r|$< 0.32, Table 6, Figure 6d). A larger amount of sea-ice and ocean surface nitrate enhances ice-PP in the JAMSTEC, UAF-R, and UW models (r = 0.47–0.76, Table 6, Figures 6e–6f), while no significant correlation is seen in the UAF-G and UVic models ($|r|$< 0.19, Table 6).

5.3. Eurasian Basin

The multi-model average of the annual total ice-PP in the Eurasian Basin shows a positive trend of 0.24 ± 0.16 mmol N m^{-2} per decade for 1980–2009 (Table 5, Figure 5a), in contrast to the Canada Basin average. However, this trend also highly relies on the contribution of 2.11 ± 0.76 mmol N m^{-2} per decade in the UW model. The UAF-G and UAF-R models in fact show significant negative trends. The trends in the JAMSTEC and UVic models are not significant. The interannual variability is out of phase among the five models (Figure 5a).

As in the western Arctic subregions, the time series of sea-ice area, snow depth, and sea-ice thickness are represented by declining trends (Table 5, Figures 5b–5d). It is likely that the enhanced inflow of warm Atlantic water from the Fram Strait plays a substantial role in the sea-ice reduction on its pathway (Polyakov et al., 2017). This change is referred to as "Atlantification." Although the SIC depression in the 2000s is most distinct in the UAF-G and UAF-R models, the annual total ice-PP is maintained at a similar level as in the 1980s and 1990s. The positive trend in the multi-model mean nitrate content seems to be a compound of different patterns from the five models (Table 5, Figures 5e–5f). The ocean surface nitrate is gradually increasing (decreasing) from 1990 to 2000 in the JAMSTEC and UW models (UAF-G, UAF-R, and UVic models). A potential factor for this discrepancy is the model bias of lateral transport. The Eurasian Basin is located along the Transpolar Drift stream from the nutrient-rich Siberian shelves to the Fram Strait and an outer part of the Beaufort Gyre centered in the Canada Basin. The shelf-basin exchange with the Barents Sea also influences biogeochemical environments in the Eurasian Basin. Since lateral flux data for nitrate are not available at the present stage, a more detailed analysis on horizontal advection is proposed as a future work.

The annual total ice-PP is linearly related to the annual peak biomass in most models (Figure 6a). The correlation coefficients in the JAMSTEC, UAF-G, UAF-R, and UVic models are quite high (r = 0.89–0.98,

Table 6). Causes for the low correlation of 0.16 in the UW model are unclear. The September SIC and spring snow depth likely have little effect on ice-PP in the five models ($|r|< 0.30$, Table 6, Figures 6b–6c). Spring thicker ice supports a positive anomaly in ice-PP ($r = 0.49$) in the JAMSTEC model, while thicker ice is a limiting factor ($r = -0.55$) in the UW model (Table 6, Figure 6d). The nitrate concentrations have a large impact on the annual total ice-PP in the JAMSTEC and UAF-G models ($r = 0.34$–0.48, Table 6, Figures 6e–6f). Correlation of the ice-PP with the ocean surface nitrate ($r = 0.72$) is clearly higher than that with the sea-ice nitrate ($r = 0.15$) in the UW model (Table 6, Figures 6e–6f). With respect to the inter-model spreads in the Eurasian Basin, the ranking of the annual total ice-PP (UW > UAF-G ~UAF-R~JAMSTEC > UVic) seems to be again controlled by V_{maxi} rather than background light and nutrient conditions as in the Canada Basin (Figure 6).

5.4. Barents Sea

The annual total ice-PP in the Barents Sea shows no significant trend (Table 5, Figure 5a). The annual minimum SIC is gradually decreasing with fluctuation in the range of 0–0.14 (Table 5, Figure 5b). The simulated snow depth, sea-ice thickness, and sea-ice nitrate show declining trends (Table 5, Figures 5c–5e). The interannual variability in these properties is quite consistent among the five models, probably because the Barents Sea averages reflect total sea-ice area in spring. Significant positive trends in the ocean surface nitrate are seen in the JAMSTEC, UAF-G, and UW models (Table 5, Figure 5f).

The Barents Sea averages also show a linear relationship between the annual total ice-PP and the annual peak biomass ($r = 0.78$–0.96) in each model (Table 6, Figure 6a). Hence, there is little regional difference of this conjunction. Thicker ice in spring enhances the annual total ice-PP in the JAMSTEC and UVic models ($r = 0.36$–0.69, Table 6, Figure 6d). The low correlation between ice-PP and ocean surface nitrate ($|r|< 0.27$), except in the UAF-R model ($r = 0.40$), might be because nitrate variability is dominated by concentrations outside the seasonal ice zone (i.e., ice-algal habitat) in the Barents Sea. In addition, it is known that silicate concentrations in the Atlantic side are lower than in the Pacific side (e.g., Garcia et al., 2013). Hence the silicate limitation may control interannual and inter-model variability in ice-PP.

5.5. Key Findings

The simulated annual peak values of sea-ice area, snow depth, and sea-ice thickness are mostly declining for 1980–2009. The spring nitrate contents at the sea ice-ocean interface show both positive and negative trends depending on the four subregions and the five models. Whereas the interannual variations in snow depth and sea-ice thickness are almost in phase in each subregion, biogeochemical variables such as the annual ice-PP and the spring nitrate contents show those peaks in different years in the five models.

The multi-model average of the annual total ice-PP is slightly increasing in the Chukchi Sea, Eurasian Basin, and Barents Sea regions but decreasing in the Canada Basin region. However, statistically significant decadal trends are hardly detected in the four subregions. Most time series of the simulated variables including the selected controlling factors are characterized by the predominant interannual variability compared with the decadal change for the analyzed three decades. The multi-model averages composed of different patterns from the five models seem not to capture typical features.

The lack of a significant correlation between the annual total ice-PP and the annual minimum SIC can be attributed to two potential reasons: First, the entire sea-ice disappearance during late summer yields little interannual variability in the minimum SIC over the seasonal sea-ice zone. Second, the mid-summer weather conditions may control sea-ice retreat after the spring ice-algal bloom. For example, the Arctic sea-ice extent was rapidly reduced by wind-driven transport associated with a dipole pattern of sea level pressure in 2007 (Wang et al., 2009) and ice-floe fragmentation under great cyclone passages in 2012 (Simmonds & Rudeva, 2012). Therefore, SIC cannot be used as a predictor of annual total ice-PP.

The simulated thicker sea ice in spring sometimes contributes to the higher annual total ice-PP, as shown by positive correlations between two properties (three cases in Table 6). On the other hand, occasional negative correlations (two cases in Table 6) indicate that thicker spring ice can be a limiting factor for the ice-PP. This contrast highlights that an appropriate balance of stable ice-algal habitat (i.e., sea-ice cover) and sufficient light penetration through the sea-ice column is necessary to keep up the ice-PP levels. A similar interpretation is applicable to the spring snow depth, which has both positive and negative correlations with the annual total ice-PP (Table 6). Whereas snow covering limits light penetration into the underlying sea-ice

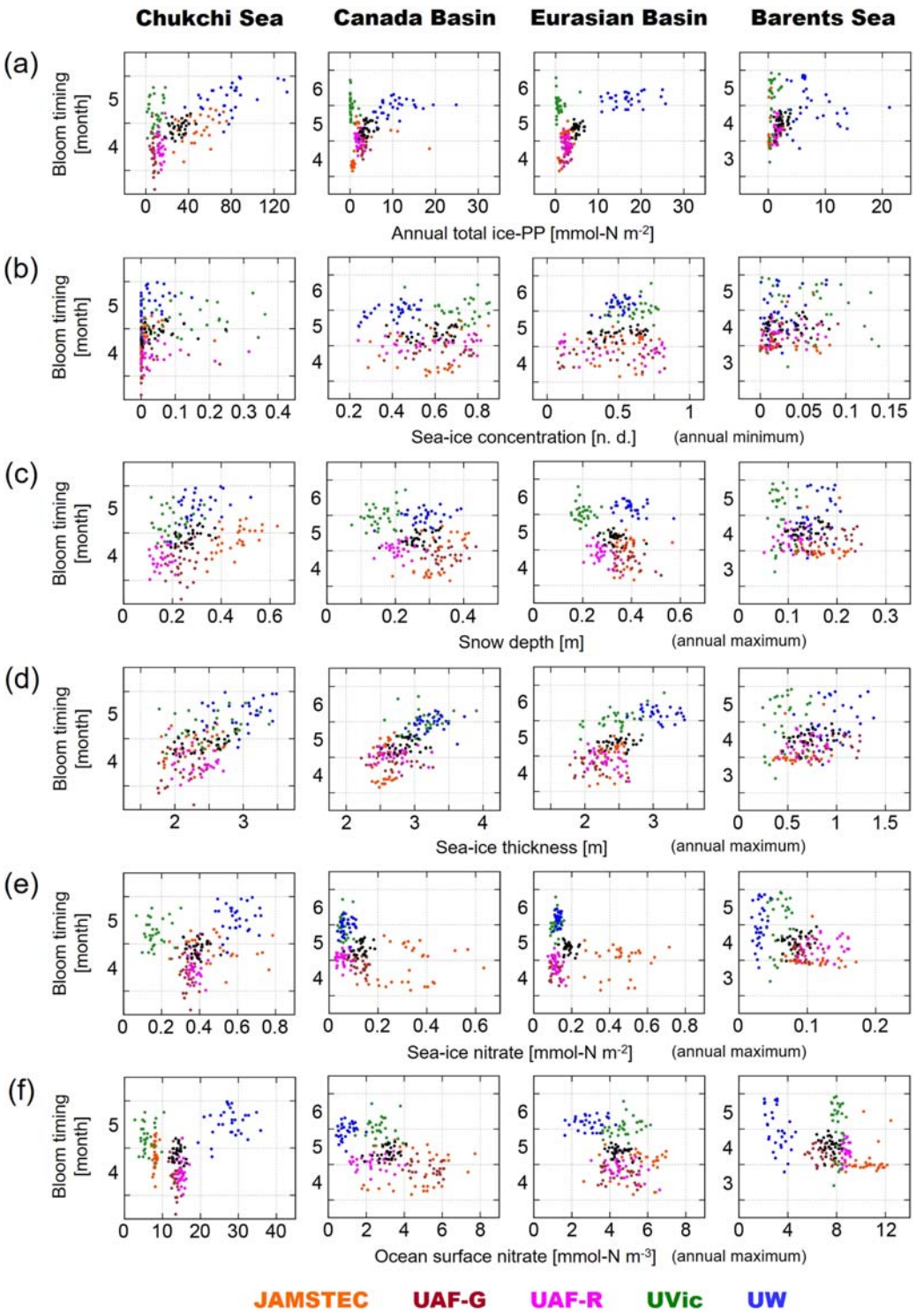

Figure 7. Relationship of bloom timing (month) with (a) ice-PP (mmol N m^{-2}), (b) sea-ice concentration (n. d.), (c) snow depth (m), (d) sea-ice thickness (m), (e) nitrate content in the sea-ice column (mmol N m^{-2}), and (f) nitrate concentration in the ocean surface layer (mmol N m^{-3}) simulated in the (orange) JAMSTEC, (brown) UAF-G, (magenta) UAF-R, (green) UVic, and (blue) UW models. The annual (a) total, (b) minimum, and (c–f) maximum averaged in the four sub-regions are shown for 1980–2009. The multi-model averages are plotted by black dots. Correlation coefficients of two properties in each model are listed in Table 7.

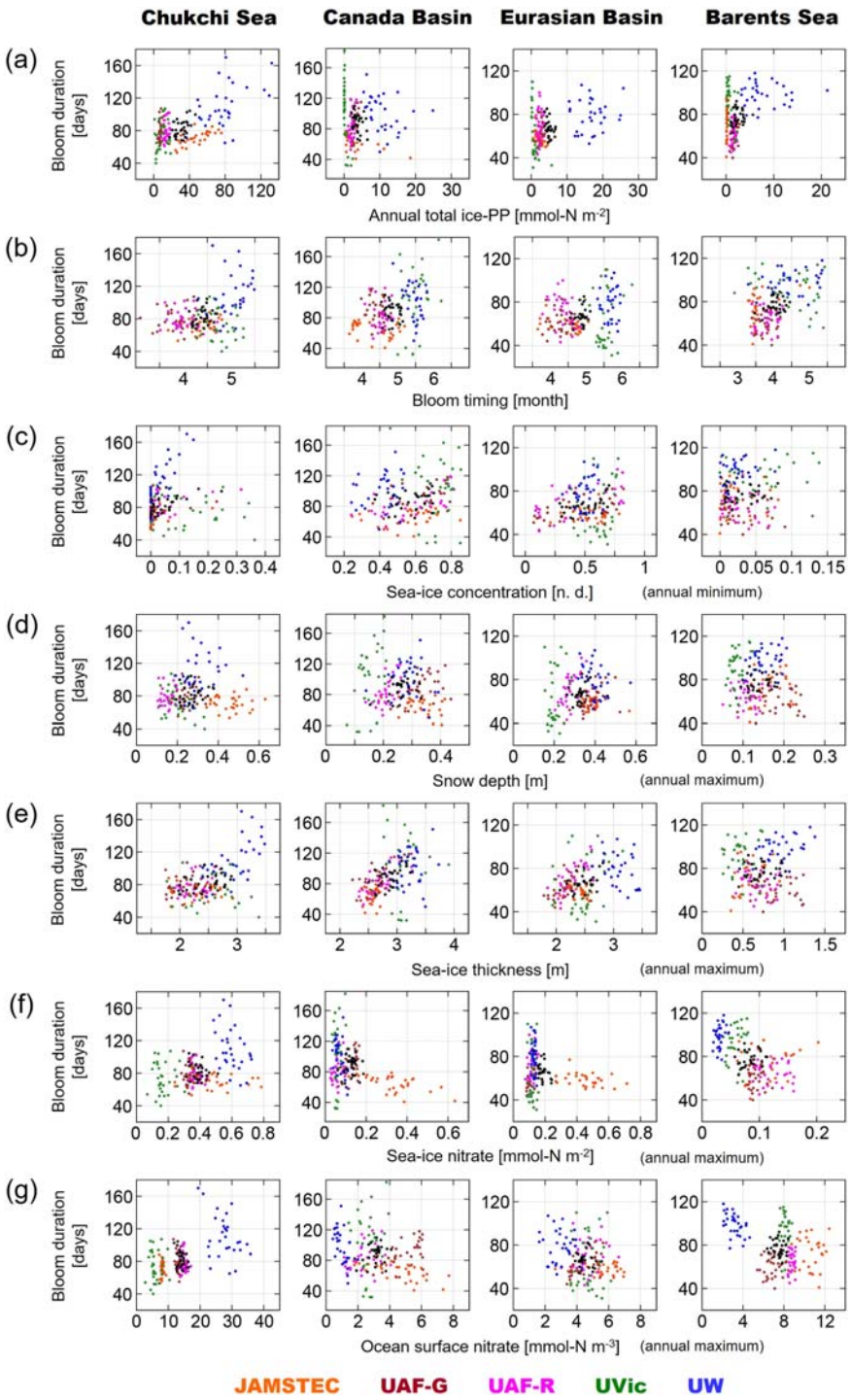

Figure 8. Relationship of bloom duration (days) with (a) ice-PP (mmol N m^{-2}), (b) bloom timing (month), (c) sea-ice concentration (n. d.), (d) snow depth (m), (e) sea-ice thickness (m), (f) nitrate content in the sea-ice column (mmol N m^{-2}), and (g) nitrate concentration in the ocean surface layer (mmol N m^{-3}) simulated in the (orange) JAMSTEC, (brown) UAF-G, (magenta) UAF-R, (green) UVic, and (blue) UW models. The annual (a) total, (c) minimum, and (d–g) maximum averaged in the four subregions are shown for 1980–2009. The multi-model averages are plotted by black dots. Correlation coefficients of two properties in each model are listed in Table 8.

Table 7
Correlation Coefficient of Bloom Timing With Annual Total Ice-PP and Annual Peak Values of Major Properties in the Four Subregions

		Multi-model average	JAMSTEC	UAF-G	UAF-R	UVic	UW
Chukchi Sea	Annual total ice-PP	0.40	0.44	−0.25	0.09	0.00	0.40
	Sea-ice concentration	0.29	0.14	−0.04	−0.06	0.09	0.15
	Snow depth	0.47	0.56	0.13	0.00	0.09	0.41
	Sea-ice thickness	0.42	0.45	0.18	−0.20	0.22	0.24
	Sea-ice nitrate	0.07	−0.16	−0.23	−0.08	0.06	0.07
	Ocean surface nitrate	0.01	0.18	−0.20	−0.15	0.05	0.20
Canada Basin	Annual total ice-PP	0.35	0.31	0.07	−0.02	−0.25	0.29
	Sea-ice concentration	0.25	0.00	0.11	0.08	−0.08	0.36
	Snow depth	0.48	0.59	−0.15	0.04	0.35	0.21
	Sea-ice thickness	0.20	0.16	−0.27	0.07	0.24	0.18
	Sea-ice nitrate	0.33	0.23	−0.33	0.01	−0.00	0.18
	Ocean surface nitrate	0.39	0.20	−0.36	−0.05	−0.05	0.27
Eurasian Basin	Annual total ice-PP	0.17	0.64	0.17	−0.10	0.14	0.22
	Sea-ice concentration	0.44	0.07	0.11	−0.33	0.36	0.46
	Snow depth	−0.24	0.08	−0.32	−0.48	−0.23	−0.33
	Sea-ice thickness	0.13	0.30	−0.20	−0.54	0.51	−0.28
	Sea-ice nitrate	−0.15	0.16	−0.16	−0.50	0.27	0.04
	Ocean surface nitrate	−0.24	0.14	−0.20	−0.45	0.33	0.13
Barents Sea	Annual total ice-PP	0.43	0.47	0.43	0.41	0.24	−0.18
	Sea-ice concentration	0.08	0.20	0.34	0.05	−0.11	0.29
	Snow depth	0.34	0.03	0.45	0.21	−0.00	0.44
	Sea-ice thickness	0.35	0.18	0.44	0.18	0.19	0.34
	Sea-ice nitrate	0.37	0.36	0.17	0.14	0.14	0.28
	Ocean surface nitrate	−0.16	0.22	−0.21	0.24	0.14	−0.48

Note. Red (blue) color means positive (negative) correlation above the 95% significant level. Yearly values are plotted in Figure 7.

column in spring, high surface albedo of snow delays loss of ice-algal habitat in the later season. The latter effect might favor the higher annual total ice-PP.

The simulated nitrate-rich precondition in spring partly enhances the annual total ice-PP, as shown by positive correlations in the central basins (five cases in Table 6). No statistically significant correlation is detected in the Chukchi Sea region, where the nitrate contents are larger relative to the other subregions. Remaining lower correlations between these properties in Table 6 suggest complex interactions due to various limiting factors and further processes (e.g., sink terms and lateral advection).

Another noticeable feature is strong conjunction between the annual total ice-PP and the spring peak biomass of ice algae in each model. Whereas the quite high correlations are robust regardless of the four subregions, the slope of linear relationship varies widely among the five models. The V_{maxi} value is a key source for the inter-model spreads of ice-PP and its ratio to the peak biomass. The fall bloom also contributes to the annual total ice-PP. However, the ice-PP integrated only for January–July has similar correlations with the spring peak biomass even in the UW model (not shown).

6. Ice-Algal Bloom Timing and Duration

Ji et al. (2013) analyzed the phenology of the ice-algal bloom and suggested that an earlier or later ice retreat had a weaker impact on the timing of the ice-algal bloom compared to the impact on the pelagic phytoplankton bloom. However, their analysis was limited to the seasonal ice zones and to the years 1998–2007, which were covered by satellite ocean color sensors. Tedesco et al. (2019) indicated a non-linear response in ice-algal phenology simulated by their sea-ice biogeochemical model against the CMIP5-derived physical variables. Therefore, it is valuable to verify these relationships using several marine ecosystem models, covering the entire Arctic Ocean over multiple decades. In the present study, timing and duration of the simulated ice-algal bloom in the four subregions are examined by analyzing key factors for their variability. The bloom

Table 8
Correlation Coefficient of Bloom Duration With Annual Total Ice-PP, Bloom Timing, and Annual Peak Values of Major Properties in the Four Subregions

		Multi-model average	JAMSTEC	UAF-G	UAF-R	UVic	UW
Chukchi Sea	Annual total ice-PP	0.50	0.66	0.41	0.32	0.21	0.48
	Bloom timing	0.27	0.45	0.03	−0.09	−0.24	0.23
	Sea-ice concentration	0.69	0.24	0.17	0.54	−0.06	0.82
	Snow depth	0.20	−0.02	0.14	0.13	−0.28	0.10
	Sea-ice thickness	0.43	−0.05	0.17	0.49	−0.05	0.59
	Sea-ice nitrate	−0.25	−0.16	0.05	−0.31	−0.00	−0.39
	Ocean surface nitrate	−0.34	−0.00	−0.14	−0.13	0.04	−0.38
Canada Basin	Annual total ice-PP	−0.32	−0.61	0.37	0.45	−0.69	−0.33
	Bloom timing	−0.12	−0.26	−0.17	0.01	0.28	−0.32
	Sea-ice concentration	0.25	0.27	0.49	0.65	−0.10	0.17
	Snow depth	0.40	−0.32	0.49	0.55	0.42	−0.09
	Sea-ice thickness	0.51	0.08	0.65	0.81	0.04	0.07
	Sea-ice nitrate	0.11	−0.60	0.54	0.39	0.25	−0.54
	Ocean surface nitrate	0.26	−0.61	0.54	0.33	0.10	−0.57
Eurasian Basin	Annual total ice-PP	−0.32	−0.47	0.39	0.18	−0.51	0.10
	Bloom timing	0.19	−0.33	0.09	−0.40	0.08	0.01
	Sea-ice concentration	0.52	0.04	0.53	0.61	0.20	0.21
	Snow depth	0.22	−0.09	0.51	0.62	0.18	−0.31
	Sea-ice thickness	0.41	−0.39	0.50	0.73	0.24	−0.35
	Sea-ice nitrate	−0.39	−0.27	0.64	0.24	0.03	−0.16
	Ocean surface nitrate	−0.21	−0.14	0.59	0.16	0.06	−0.07
Barents Sea	Annual total ice-PP	0.16	0.38	0.46	0.33	−0.46	−0.02
	Bloom timing	0.22	0.44	0.08	0.13	−0.30	0.25
	Sea-ice concentration	0.09	0.01	−0.26	−0.21	0.07	0.34
	Snow depth	0.22	0.24	−0.01	−0.07	0.26	0.23
	Sea-ice thickness	0.17	0.28	−0.08	−0.18	0.06	0.41
	Sea-ice nitrate	0.25	0.34	−0.11	−0.12	0.26	0.37
	Ocean surface nitrate	−0.12	0.04	0.11	0.12	0.09	−0.48

Note. Red (blue) color means positive (negative) correlation above the significant level. Yearly values are plotted in Figure 8.

timing is defined by a peak date of the ice-PP averaged in the subregions in each year. The bloom duration is defined by total days when the ice-PP is higher than 10% of the annual peak value in each year in each subregion. The fall bloom contribution is excluded by evaluating the daily ice-PP only for January–July. The multi-model average in each year is then calculated based on the respective bloom timing and duration for each model, not based on the averaged ice-PP. Relationships of the bloom timing and duration with the annual peak values of the same properties chosen in section 5 are examined using the scatter plots (Figures 7 and 8) with the Pearson correlation coefficients (r) of interannual variability (Tables 7 and 8) as a means of measure. To facilitate easier interpretation of changes in the simulated bloom duration and magnitude, we introduce four types of the seasonal transition in regionally averaged ice-PP: (A) long-massive, (B) short-massive, (C) long-gentle, and (D) short-gentle characteristics shown in Figure 9. Note that these types are not specific ecological categories based on physiological response, and thus no exact definition is required.

6.1. Chukchi Sea

The peak timing of the ice-PP is gradually shifting to an earlier date in the Chukchi Sea (Figure 5g). The multi-model average is from late April to early May and shifts by -2.02 ± 0.93 day per decade for 1980–2009 (Table 5). The peak timing interannually varies within a month for each model and within 2 months (late March–late May) among the five models (Figures 5g and 6). The correlation with the annual minimum SIC is quite low ($|r| < 0.15$, Table 7, Figure 7b) for the same reasons described in section 5.1. The heavy snow cover delays the ice-PP peak in the JAMSTEC and UW models ($r = 0.41$–0.56, Table 7, Figure 7c). The correlation with the sea-ice thickness is significant only in the JAMSTEC model ($r = 0.45$, Table 7, Figure 7d). These relationships are not detected in the UAF-G, UAF-R, and UVic models (Table 8, Figures 8c–8d). The nitrate contents hardly control the bloom timing in any models ($|r| < 0.23$, Table 7, Figures 8e–8f). Therefore,

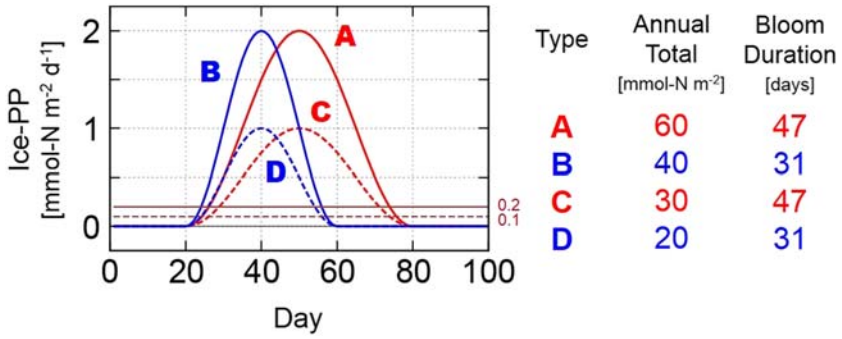

Figure 9. Schematic image of four bloom types: (A) long-massive, (B) short-massive, (C) long-gentle, and (D) short-gentle characteristics. When these types are plotted using sine curves, the annual total ice-PP decreases from type A to type D. The bloom duration defined in section 6 (brown lines correspond to threshold values) is longer in the types A and C than in the types B and D. The numbers of the annual total ice-PP (mmol N m^{-2}) and bloom duration (days) are examples calculated from this qualitative illustration. The onset and peak timings are not categorized in the four types.

it is suggested that the simulated bloom shift can be caused by a decline in spring snow depth and sea-ice thickness rather than nutrient availability. The positive correlation between the annual total ice-PP and bloom timing in the JAMSTEC and UW models (r = 0.40–0.44, Table 7, Figure 7a) indicates that an earlier spring bloom is linked with smaller annual total ice-PP. With respect to the inter-model spreads in multi-decadal averages, the bloom timing is sensitive to the maximum sea-ice thickness: The later ice-PP peak appears in the UW and UVic models, where the thicker ice directly impacts light limitation during the spring bloom (Figure 7d).

The bloom duration is also decreasing in all five models (Figure 5h). The multi-model average is around 80 days and has a significant trend of −6.81 ± 1.76 days per decade for 1980–2009 (Table 5). It should be noted that the bloom duration in an individual grid of each model is much shorter than that calculated from the regionally averaged ice-PP, since the bloom starts and ends at different times even within each subregion. The largest significant negative trend of −17.07 ± 4.61 days per decade is simulated in the UW model (Table 5). Smaller values of the bloom duration mean that increment and/or decline curves of the daily ice-PP seasonal transition are steeper (types B and D in Figure 9). In the UAF-R and UW models, thinner sea ice and greater nitrate contents favor a shorter bloom (Table 8, Figures 8e–8g), because less limitation factors promote speedy ice-algal growth (i.e., steeper increment curve). In addition, the rapid sea-ice melt terminates the spring bloom quickly (i.e., steeper decline curve). In the Chukchi Sea, the shorter bloom leads to a reduction in the annual total ice-PP (Figure 8a), as shown in the positive correlations for most models (r = 0.21–0.66, Table 8, Figure 8a). This simulated change is illustrated by a transition from type A to B or D (Figure 9).

6.2. Canada Basin

The ice-PP peak in the Canada Basin occurs a few weeks later than the Chukchi Sea average. The multi-model average of the bloom timing in the Canada Basin starts in mid-May (Figure 5g) and shifts by −2.80 ± 1.02 day per decade (Table 5). The correlation with the minimum SIC is still low ($|r| < 0.11$, Table 7), except the UW model ($r = 0.36$, Table 7), even though the interannual variability is clear in contrast to the Chukchi Sea region (Figures 5b and 6b). The high correlation is generated from the snow depth simulated by the JAMSTEC model ($r = 0.59$, Table 7, Figure 7c). The recent nutricline deepening in the Canada Basin may have led to a delay in the spring bloom as in the UAF-G model ($r = -0.36$, Table 7, Figure 7f). It is also found that a simulated earlier spring bloom rarely boosts the annual total ice-PP (i.e., no significant negative correlation, Table 7, Figure 7a), as well as the Chukchi Sea. The earlier peak in spring potentially arises from a sudden and rapid loss of ice algae via meltwater flushing, which is not analyzed in the present study. The annual total ice-PP is theoretically speculated to reach the highest levels, if the habitat loss starts after the required nutrients are depleted. As in the Chukchi Sea, the bloom timing is highly sensitive to the spring sea-ice thickness with respect to the inter-model spreads (Figure 7d). Higher nitrate concentrations in the ocean surface layer also seem to induce an earlier bloom in the Canada Basin (Figure 7f). However, it is

possible that the ocean surface nitrate happens to be large in the models producing thinner ice (e.g., the JAMSTEC and UAF-G models).

The decadal mean bloom duration in the Canada Basin is close to the Chukchi Sea average (Figure 5h). The UW model shows a significant positive trend of 11.59 ± 4.43 days per decade (Table 5). The decline in nitrate availability on the decadal timescale can account for this longer bloom (Figures 5e–5f), as supported by negative correlations ($r = -0.54$ for sea-ice nitrate, $r = -0.57$ for ocean surface nitrate, Table 8, Figures 8f–8g) in the UW model. This change is illustrated by the bloom-type shift from B to C (Figure 9). Similar correlations appear in the JAMSTEC model ($r = -0.60$ for sea-ice nitrate, $r = -0.61$ for ocean surface nitrate, Table 8), although no significant nitrate trends for 1980–2009 are simulated (Table 5, Figures 5e–5f). In contrast, the bloom duration becomes shorter in the UAF-G and UAF-R models (Table 5, Figure 5h). In these models, all the annual peak values of sea-ice concentration, snow depth, sea-ice thickness, and nitrate contents have positive correlations with the bloom duration ($r = 0.33$–0.81, Table 8, Figures 8c–8g). It is reasonable in this case that limited ice-algal growth and enhanced loss through melting contribute to the bloom shortening like the type shift from A to D (Figure 9). The strong negative correlations between the bloom duration and the annual total ice-PP, which appear in the JAMSTEC and UVic models ($|r| = 0.61$–0.69, Table 8, Figure 8a), are obtained by a combination of short-massive (type B) and long-gentle (type C) blooms. With respect to the inter-model spreads, the bloom duration has little relationship with potential controlling factors (Figure 8). It should be noted that the widest range of 32–182 days is simulated in the UVic model, which produces the lowest ice-PP (Figures 5a, 5h, and 8).

6.3. Eurasian Basin

The bloom timing in the Eurasian Basin is close to the Canada Basin average (i.e., mid-May), and the multi-model average trend is −1.16 ± 0.84 day per decade (Table 5, Figure 5g). The high positive correlation with the SIC (sea-ice thickness) appears in the UW (UVic) model, respectively ($r = 0.46$–0.51, Table 7, Figures 7b and 7d). On the other hand, correlation coefficients between the bloom timing and major background properties are significantly negative ($|r| = 0.45$–0.54, Table 7, Figures 7b–7f) in the UAF-R model. The UAF-G model produces a similar relationship with lower negative correlation ($|r| = 0.16$–0.32, Table 7, Figures 7b–7f). It is counterintuitive that heavy snow, thicker ice, and lower nitrate concentrations are simulated at the earlier ice-PP peaks. The sink terms of ice-algal biomass budget such as mortality and melt loss (i.e., (3)–(6) in section 3) might quickly exceed the limited source term due to less light and nutrient availability for ice-algal growth. The ice-PP peaks in the UVic and UW models are later than those in the JAMSTEC, UAF-G, and UAF-R models throughout the target period of 1980–2009 (Figure 5g). This lag of several weeks is most obvious in the Eurasian Basin. In this connection, a close relationship between the bloom timing and the annual total ice-PP is undetectable in the inter-model spreads (Figure 7a).

The bloom duration in the Eurasian Basin is a few weeks shorter than in the Chukchi Sea and Canada Basin (Figure 5h), and the five models produce contrasting decadal trends (Table 5). Small positive trends are simulated in the JAMSTEC and UW models, where the bloom duration has a weak negative correlation with the spring sea-ice thickness ($|r| = 0.35$–0.39, Table 8, Figure 8e). Hence, sea-ice thinning works toward the longer bloom in this case (i.e., the type shift from D to A). The increase in the ocean surface nitrate has little impact on the bloom duration in the JAMSTEC and UW models ($|r| = 0.07$–0.14, Table 8, Figure 8g). The significant negative trends in the bloom duration and its correlations with background conditions shown in the UAF-G and UAF-R models are similar to those in the Canada Basin (Tables 5 and 8, Figures 8c–g).

6.4. Barents Sea

The earliest ice-PP peaks are produced in the Barents Sea (Figure 5g). The multi-model average is April in most years and shifts with a trend of −1.44 ± 1.36 day per decade (Table 5). The declines in spring snow depth and sea-ice thickness hasten the bloom timing in the UAF-G model ($r = 0.44$–0.45, Tables 5 and 7, Figures 7c–7d). A similar relationship with snow depth appears in the UW model ($r = 0.44$, Table 7, Figure 7c). The positive correlation with the sea-ice nitrate is triggered by an extreme annual peak of 0.20 mmol N m^{-2} in the JAMSTEC model ($r = 0.36$, Table 7, Figure 7e). When this peak is excluded, the correlation is reduced to 0.02. The interannual variability in bloom timing ranges over 2 months in the UVic and UW models, even though major background properties have similar ranges in the five models (Figure 7).

The bloom duration in the Barents Sea is close to the Chukchi Sea average, and a significant negative trend of -5.20 ± 1.98 days per decade is simulated only in the UW model (Table 5, Figure 5h). The sea-ice thinning induces the shorter bloom in the UW model ($r = 0.41$, Table 8, Figure 8e). The UVic model produces a strong negative correlation between the bloom duration and the annual total ice-PP ($r = -0.46$, Table 8, Figure 8a), as in the central basins ($|r| = 0.51$–0.69, Table 8, Figure 8a). On the other hand, the smaller ice-PP is accompanied by a shorter bloom in the JAMSTEC and UAF-G models ($r = 0.38$–0.46, Table 8, Figure 8a). These changes are illustrated by a shift from bloom type C to B (A to D) in the former (latter) case, respectively (Figure 9). Overall, a significant linkage between the bloom timing and duration is detected only in the JAMSTEC model, where a shorter bloom occurs in earlier spring in the Chukchi Sea and Barents Sea ($r = 0.44$–0.45, Table 8, Figure 8b), and in later spring with lower correlations for the central basins ($|r| = 0.26$–0.33, Table 8, Figure 8b).

6.5. Key Findings

The ice-PP peak in the Chukchi Sea and Barents Sea regions appears several weeks earlier than in the Canada and Eurasian Basins (Figure 5g). The bloom timing in each subregion interannually fluctuates within 2 months for each model, and the decadal averages vary within 2 months among the five models. The spring ice-algal bloom gradually shifts to an earlier date in all four subregions, especially in the Canada Basin. The correlation with the annual minimum SIC is low for reasons described in section 5.5, except the UW model in the central basins. A simulated earlier bloom can be caused by a relaxation of the light limitation, due to thinner snow and sea ice, whereas the nutricline deepening delays the bloom timing in the Canada Basin. The bloom duration is comparable among the Chukchi Sea, Canada Basin, and Barents Sea regions and is somewhat shorter in the Eurasian Basin. The bloom duration mostly shortens over the three decades in all five models.

With respect to the inter-model spread, the bloom timing is sensitive to spring sea-ice thickness. A later ice-PP peak appears in the UVic and UW models, which produce thicker spring ice directly and hence limited light availability. The bloom duration seems to have little linkage with the assessed factors. In the central basins, the widest range of the bloom duration is simulated in the UVic model, which produces the lowest -ice-PP.

A simulated earlier spring bloom is sometimes linked with lower annual total ice-PP, as suggested by positive correlations between two properties (Table 7). This relationship is illustrated by a type shift from A to B or D (Figure 9). Preconditioning with less nutrient availability and/or more rapid release of ice algae driven by massive meltwater flushing can terminate the spring bloom earlier and cause corresponding reduction in both the bloom duration and the annual total ice-PP. On the other hand, it is possible that a shorter bloom is achieved by larger nitrate contents due to a steeper increment curve of the ice-PP seasonal transition. A type shift from C to B (Figure 9) also appears, when the sink terms in the ice-algal biomass budget such as mortality and melt loss (i.e., (3)–(6) in section 2.5) exceed the enhanced photosynthesis term in an earlier month. Thus, the simulated bloom features are complicated, and various type shifts due to different mechanisms are detected among the four subregions and among the five models, respectively. The evaluation of total ice-algal biomass budget, which is out of the scope of the present study, will be an important future task.

7. Conclusions and Future Works

A multi-model intercomparison of pan-Arctic ice-algal productivity (ice-PP) was conducted within the framework of the FAMOS project. In particular, the seasonal, interannual, and decadal variations for 1980–2009 in the four subregions (Chukchi Sea, Canada Basin, Eurasian Basin, and Barents Sea) were discussed. The spatial distributions of annual total ice-PP simulated by the five regional or global sea ice-ocean models are characterized by a shelf-basin contrast. A higher annual total ice-PP is simulated in the Chukchi Sea, the Laptev Sea, and the Canadian Polar Shelf due to a combination of thinner sea ice and nutrient-rich conditions relative to those in the central basin region. These models qualitatively reproduce seasonal cycles of snow, sea-ice, and ocean properties which impact ice algae, but the amplitudes of ice-PP and these properties substantially vary among the four subregions and among the five models, respectively.

The simulated annual total ice-PP shows no common decadal trend at least for 1980–2009 among the five models, although the simulated snow depth and sea-ice thickness are mostly declining over the time

period. This relationship is similar to the disagreement of long-term trends in under-ice phytoplankton PP among three models, which was suggested in Jin et al. (2016). The correlations with the annual minimum sea-ice area in each subregion are quite low, possibly because the September sea-ice cover is regulated by mid-summer weather conditions occasionally producing wind-driven sea-ice retreat after the spring ice-algal bloom. The model intercomparison indicates that an appropriate balance of a stable ice-algal habitat (i.e., sea-ice cover) and sufficient light penetration to the sea ice-ocean interface is necessary to retain ice-PP. The models suggest that the interannual variability in ice-PP is clearly larger than the decadal trend owing to complex interactions among various limiting factors. Another feature in the interannual variability is a linear relationship of the annual total ice-PP with the annual peak biomass of ice algae in each subregion, even though the slope of the relationship varies widely among the five models.

The timing of the simulated ice-algal bloom is a few weeks earlier in the Chukchi Sea and Barents Sea regions than in the central basins. The multi-model averages show that the ice-algal bloom is gradually shifting toward an earlier date in the four subregions, especially in the Canada Basin. The simulated earlier bloom is more likely caused by declines in spring snow depth and sea-ice thickness than by nutrient variability. The reduction in the annual total ice-PP is occasionally accompanied by an earlier spring bloom. The simulated bloom duration mostly shortens for the three decades in the four subregions. However, the correlation of the bloom duration with snow, sea-ice, and ocean properties related to ice algae varies widely among the four subregions and among the five models, respectively. It is plausible that a more rapid loss through melting terminates the spring bloom earlier. There appear to be various types of seasonal transition in regionally averaged ice-PP: long-massive, short-massive, long-gentle, and short-gentle features for 1980–2009 in the five models.

The sea-ice duration in each year is a key index controlling the ice-PP. For example, the annual sea-ice duration defined using the SIC >0.15 is within 1 month in the Nordic seas except the East Greenland Current pathway (not shown). No ice-algal bloom is simulated when sea ice exists only during the polar night period. On the other hand, the sea-ice duration, which is approximately half year at the Bering Strait, is still much longer than the simulated bloom duration in the four subregions. If sea ice retreats earlier under a possible warming climate in the future, weaker solar radiation before earlier loss of ice-algal habitat will strongly restricts ice-PP as in the Nordic seas.

Some specific features in the individual models are noted. In the JAMSTEC model, moderate sea-ice thickness and higher nitrate availability assist the ice-PP in spite of a higher snow cover. In the UAF models, the ratio of the annual total ice-PP to the annual peak biomass of ice algae is low. The shelf-basin contrast of ice-PP and ocean surface nitrate is more vivid in the high-resolution regional version (UAF-R) relative to the low-resolution global version (UAF-G). In the UVic model, the thicker sea ice and lower availability of sea-ice nitrate lead to a lower ice-PP and later bloom timing. The UW model reaches the highest ice-PP due to a larger maximum rate of ice-algal growth (V_{maxi}) per unit biomass.

With respect to the inter-model spreads, the annual total ice-PP depends more strongly on the V_{maxi} value rather than on background light and nutrient conditions. The simulated ice-PP is regulated not only by the photosynthesis terms but also by the loss processes (e.g., mortality and melting) and lateral advection, which are not compared in the present study. For example, a high sensitivity of the ice-algal bloom to mortality terms was reported in Mortenson et al. (2017). The evaluation of all elements in the ice-algal biomass budget would further improve the understanding of the ice-PP characteristics.

At this stage confident validation of annual total ice-PP is difficult, because observational data covering pan-Arctic and decadal scales are highly limited. Note that the in situ ice-PP estimate is different between ^{14}C incubation and oxygen-based methods (McMinn & Hegseth, 2007). Many uncertainties still remain with respect to ice-algal model parameterizations, for example, photo-acclimation, nutrient uptake, seeding to phytoplankton, zooplankton grazing pressure, and assemblage sinking speed (Steiner et al., 2016). International studies on sea-ice biogeochemistry are progressing within the research community on Biogeochemical Exchange Processes at the Sea-Ice Interfaces (BEPSII) (e.g., Steiner & Stefels, 2017) and on Measuring Essential Climate Variables in Sea Ice (ECV-Ice). The physiological response to future climate changes may differ among a couple of functional algal groups (e.g., pennate diatom, centric diatom, flagellate, and sub-ice strands) (van Leeuwe et al., 2018). The impact of multi-layer habitats influenced by brine

dynamics and pressure ridging/rafting (Vancoppenolle, Meiners, et al., 2013) on basin-scale ice-PP requires better understanding. Continuous in situ and laboratory measurements to better constrain model formulation and parameter values would be helpful to achieve more consistency among the models. There is even less quantitative data for the fall bloom magnitude, which affects an accurate estimation of annual total ice-PP. Collaborative work with long-term field expeditions such as represented by the Multidisciplinary drifting Observatory for the Study of Arctic Climate (MOSAiC) for 2019–2020 are highly valuable for comprehensive understanding of sea-ice biogeochemical processes.

Acknowledgments

E. W. is supported by the Grant-in-Aid for Scientific Research of Japan Society for the Promotion of Science (JSPS) (KAKENHI 18H03368) and the Arctic Challenge for Sustainability (ArCS) project funded by the Ministry of Education, Culture, Sports, Science and Technology (MEXT), Japan. M. J. is supported by NSF Office of Polar Programs (OPP) Grant (PLR-1417925). H. H. and N. S. acknowledge funding from the Canadian Network on Climate and Aerosols in Remote Environments (NETCARE), Fisheries and Oceans Canada. J. Z. is supported by NASA Grants (NNX17AD27G, NNX15AG68G) and NSF OPP Grants (PLR-1416920 and PLR-1603259). The JAMSTEC and UVic model experiments were executed using the JAMSTEC Earth Simulator and the Compute Canada-Westgrid, respectively. The daily time series of the ice-PP, ice-algal biomass, sea-ice concentration, snow depth, sea-ice thickness, sea-ice nitrate, and ocean surface nitrate for 1980–2009 produced by the five models are available at the Arctic Data Archive System (https://ads.nipr.ac.jp/dataset/A20190924-001). This study is a contribution to the Forum for Arctic Modelling and Observational Synthesis (FAMOS) and the research community on Biogeochemical Exchange Processes at the Sea-Ice Interfaces (BEPSII). Finally, thoughtful and constructive comments from two anonymous referees were highly valuable.

References

Arora, V. K., Scinocca, J. F., Boer, G. J., Christian, J. R., Denman, K. L., Flato, G. M., et al. (2011). Carbon emission limits required to satisfy future representative concentration pathways of greenhouse gases. *Geophysical Research Letters*, 38. https://doi.org/10.1029/2010GL046270

Arrigo, K. R., Kremer, J. N., & Sullivan, C. W. (1993). A simulated Antarctic fast ice ecosystem. *Journal of Geophysical Research*, *98*, 6929–6946. https://doi.org/10.1029/93jc00141

Arrigo, K. R., & van Dijken, G. L. (2015). Continued increases in Arctic Ocean primary production. *Progress in Oceanography*, *136*, 60–70. https://doi.org/10.1016/j.pocean.2015.05.002

Årthun, M., Eldevik, T., Smedsrud, L. H., Skagseth, Ø., & Ingvaldsen, R. B. (2012). Quantifying the influence of Atlantic heat on Barents Sea ice variability and retreat. *Journal of Climate*, *25*, 4736–4743. https://doi.org/10.1175/JCLI-D-11-00466.1

Assmy, P., Ehn, J. K., Fernández-Méndez, M., Hop, H., Katlein, C., Sundfjord, A., et al. (2013). Floating ice-algal aggregates below melting Arctic sea ice. *PLoS ONE*, *8*(10), e76599. https://doi.org/10.1371/journal.pone.0076599

Balmaseda, M. A., Mogensen, K., & Weaver, A. T. (2013). Evaluation of the ECMWF ocean reanalysis system ORAS4. *Quarterly Journal of the Royal Meteorological Society*, *139*, 1132–1161. https://doi.org/10.1002/qj.2063

Bitz, C. M., Holland, M. M., Weaver, A. J., & Eby, M. (2001). Simulating the ice-thickness distribution in a coupled climate model. *Journal of Geophysical Research*, *106*, 2441–2463. https://doi.org/10.1029/1999jc000113

Bitz, C. M., & Lipscomb, W. H. (1999). An energy-conserving thermodynamic model of sea ice. *Journal of Geophysical Research*, *104*, 15,669–15,677. https://doi.org/10.1029/1999jc900100

Boetius, A., Albrecht, S., Bakker, K., Bienhold, C., Felden, J., Fernández-Méndez, M., et al., & RV Polarstern ARK27-3-Shipboard Science Party (2013). Export of algal biomass from the melting Arctic sea ice. *Science*, *339*(6126), 1430–1432. https://doi.org/10.1126/science.1231346

Castellani, G., Losch, M., Lange, B. A., & Flores, H. (2017). Modeling Arctic sea-ice algae: Physical drivers of spatial distribution and algae phenology. *Journal of Geophysical Research: Oceans*, *122*, 7466–7487. https://doi.org/10.1002/2017JC012828

Corlett, W. B., & Pickart, R. S. (2017). The Chukchi slope current. *Progress in Oceanography*, *153*, 50–65. https://doi.org/10.1016/j.pocean.2017.04.005

Deal, C., Jin, M., Elliott, S., Hunke, E., Maltrud, M., & Jeffery, N. (2011). Large-scale modeling of primary production and ice algal biomass within arctic sea ice in 1992. *Journal of Geophysical Research*, *116*, C07004. https://doi.org/10.1029/2010JC006409

Dee, D. P., Uppala, S. M., Simmons, A. J., Berrisford, P., Poli, P., Kobayashi, S., et al. (2011). The ERA-Interim reanalysis: Configuration and performance of the data assimilation system. *Quarterly Journal of the Royal Meteorological Society*, *137*, 553–597. https://doi.org/10.1002/qj.828

Dupont, F. (2012). Impact of sea-ice biology on overall primary production in a biophysical model of the pan-Arctic Ocean. *Journal of Geophysical Research*, *117*, C00D17. https://doi.org/10.1029/2011JC006983

Dussin, R., Barnier, B., Brodeau, L., & Molines, J. M. (2016). The making of the Drakkar Forcing Set DFS5. DRAKKAR/MyOcean Rep. 01–04,16, Laboratoire de glaciologie et géophysique de l'environnement (LGGE), Grenoble, France.

Fernández-Méndez, M., Wenzhöfer, F., Peeken, I., Sørensen, H. L., Glud, R. N., & Boetius, A. (2014). Composition, buoyancy regulation and fate of ice algal aggregates in the central Arctic Ocean. *PLoS ONE*, *9*(9), e107452. https://doi.org/10.1371/journal.pone.0107452

Fichefet, T., & Maqueda, M. A. M. (1997). Sensitivity of a global sea ice model to the treatment of ice thermodynamics and dynamics. *Journal of Geophysical Research*, *102*, 12,609–12,646. https://doi.org/10.1029/97JC00480

Garcia, H. E., Locarnini, R. A., Boyer, T. P., & Antonov, J. I. (2006). Nutrients (phosphate, nitrate, silicate). In S. Levitus (Ed.), *World Ocean Atlas 2005*, (Vol. 4, p. 64). NOAA Atlas NESDIS. 396 pp.

Garcia, H. E., Locarnini, R. A., Boyer, T. P., Antonov, J. I., Baranova, O. K., Zweng, M. M., et al. (2013). Dissolved inorganic nutrients (phosphate, nitrate, silicate). In S. Levitus (Ed.), Mishonov, A. Technical Ed.*World Ocean Atlas 2013*, (Vol. 4, p. 76). NOAA Atlas NESDIS. 25 pp.

Gosselin, M., Levasseur, M., Wheeler, P. A., Horner, R. A., & Booth, B. C. (1997). New measurements of phytoplankton and ice algal production in the Arctic Ocean. *Deep–Sea Research Part II*, *44*, 1623–1644. https://doi.org/10.1016/s0967-0645(97)00054-4

Gradinger, R. (2009). Sea-ice algae: Major contributors to primary production and algal biomass in the Chukchi and Beaufort Seas during May/June 2002. *Deep–Sea Research Part II*, *56*, 1201–1212. https://doi.org/10.1016/j.dsr2.2008.10.016

Hasumi, H. (2006). CCSR Ocean Component Model (COCO) version 4.0. *Center for Climate System Research Report No. 25*, *Univ. of Tokyo*. 103 pp.

Hayashida, H. (2018). Modelling sea-ice and oceanic dimethylsulfide production and emissions in the Arctic, PhD thesis. Victoria, BC, Canada: University of Victoria. http://dspace.library.uvic.ca/handle/1828/10486

Hayashida, H., Christian, J. R., Holdsworth, A. M., Hu, X., Monahan, A. H., Mortenson, E., et al. (2019). CSIB v1: A sea-ice biogeochemical model for the NEMO community ocean modelling framework. *Geoscientific Model Development*, *12*, 1965–1990. https://doi.org/10.5194/gmd-12-1965-2019

Hayashida, H., Steiner, N., Monahan, A., Galindo, V., Lizotte, M., & Levasseur, M. (2017). Implications of sea-ice biogeochemistry for oceanic production and emissions of dimethyl sulfide in the Arctic. *Biogeosciences*, *14*, 3129–3155. https://doi.org/10.5194/bg-14-3129-2017

Hu, X., & Myers, P. G. (2013). A Lagrangian view of Pacific water inflow pathways in the Arctic Ocean during model spin-up. *Ocean Modelling*, *71*, 66–80. https://doi.org/10.1016/j.ocemod.2013.06.007

Hunke, E. C., & Dukowicz, J. K. (1997). An elastic-viscous-plastic model for sea ice dynamics. *Journal of Physical Oceanography*, *27*, 1849–1867. https://doi.org/10.1175/1520-0485(1997)027<1849:AEVPMF>2.0.CO;2

Hunke, E. C., Hebert, D. A., & Lecomte, O. (2013). Level-ice melt ponds in the Los Alamos sea ice model, CICE. *Ocean Modelling*, *71*, 26–42. https://doi.org/10.1016/j.ocemod.2012.11.008

Ji, R., Jin, M., & Varpe, Ø. (2013). Sea ice phenology and timing of primary production pulses in the Arctic Ocean. *Global Change Biology*, *19*(3), 734–741. https://doi.org/10.1111/gcb.12074

Jin, M., Deal, C., Lee, S. H., Elliott, S., Hunke, E., Maltrud, M., & Jeffery, N. (2012). Investigation of Arctic sea ice and ocean primary production for the period 1992-2007 using a 3-D global ice-ocean ecosystem model. *Deep–Sea Research Part II*, *81–84*, 28–35. https://doi.org/10.1016/j.dsr2.2011.06.003

Jin, M., Deal, C., Maslowski, W., Matrai, P., Roberts, A., Osinski, R., et al. (2018). Effects of model resolution and ocean mixing on forced ice-ocean physical and biogeochemical simulations using global and regional system models. *Journal of Geophysical Research: Oceans*, 123. https://doi.org/10.1002/2017JC013365

Jin, M., Deal, C. J., Wang, J., Shin, K.-H., Tanaka, N., Whitledge, T. E., et al. (2006). Controls of the landfast ice-ocean ecosystem offshore Barrow, Alaska. *Annals of Glaciology*, *44*, 63–72. https://doi.org/10.3189/172756406781811709

Jin, M., Hutchings, J., Kawaguchi, Y., & Kikuchi, T. (2012). Ocean mixing with lead-dependent subgrid scale brine rejection parameterization in a climate model. *Journal of Ocean University of China*, *11*(4), 473–480. https://doi.org/10.1007/s11802-012-2094-4

Jin, M., Popova, E. E., Zhang, J., Ji, R., Pendleton, D., Varpe, Ø., et al. (2016). Ecosystem model intercomparison of under-ice and total primary production in the Arctic Ocean. *Journal of Geophysical Research: Oceans*, *121*, 934–948. https://doi.org/10.1002/2015JC011183

Kishi, M. J., Kashiwai, M., Ware, D. M., Megrey, B. A., Eslinger, D. L., Werner, F. E., et al. (2007). NEMURO—A lower trophic level model for the North Pacific marine ecosystem. *Ecological Modelling*, *202*, 12–25. https://doi.org/10.1016/j.ecolmodel.2006.08.021

Large, W. G., & Yeager, S. G. (2009). The global climatology of an interannually varying air-sea flux data set. *Climate Dynamics*, *33*, 341–364 . https://doi.org/10.1007/s00382-008-0441-3

Lauvset, S. K., Key, R. M., Olsen, A., van Heuven, S., Velo, A., Lin, X., et al. (2016). A new global interior ocean mapped climatology: The 1° × 1° GLODAP version 2. *Earth System Science Data*, *8*, 325–340. https://doi.org/10.5194/essd-8-325-2016

Lavoie, D., Denman, K., & Michel, C. (2005). Modeling ice algal growth and decline in a seasonally ice-covered region of the Arctic (Resolute Passage, Canadian Archipelago). *Journal of Geophysical Research*, *110*, C11009. https://doi.org/10.1029/2005JC002922

Laxon, S. W., Giles, K. A., Ridout, A. L., Wingham, D. J., Willatt, R., Cullen, R., et al. (2013). CryoSat-2 estimates of Arctic sea ice thickness and volume. *Geophysical Research Letters*, *40*, 732–737. https://doi.org/10.1002/grl.50193

Lee, Y. J., Matrai, P. A., Friedrichs, M. A. M., Saba, V. S., Aumont, O., Babin, M., et al. (2016). Net primary productivity estimates and environmental variables in the Arctic Ocean: An assessment of coupled physical-biogeochemical models. *Journal of Geophysical Research: Oceans*, *121*, 8635–8669. https://doi.org/10.1002/2016JC011993

Legendre, L., Ackley, S. F., Dieckmann, G. S., Gullicksen, B., Horner, R., Hoshiai, T., et al. (1992). Ecology of sea ice biota: Part 2. Global significance. *Polar Biology*, *12*, 429–444. https://doi.org/10.1007/BF00243114

Leu, E., Mundy, C. J., Assmy, P., Campbell, K., Gabrielsen, T. M., Gosselin, M., et al. (2015). Arctic spring awakening—Steering principles behind the phenology of vernal ice algal blooms. *Progress in Oceanography*, *139*, 151–170. https://doi.org/10.1016/j.pocean.2015.07.012

Lindsay, R., & Schweiger, A. J. (2013), updated 2017). *Unified sea ice thickness climate data record, 1947 Onward, Version 1. Boulder, Colorado USA*. NSIDC: National Snow and Ice Data Center. https://doi.org/10.7265/N5D50JXV

Lipscomb, W. H. (2001). Remapping the thickness distribution in sea ice models. *Journal of Geophysical Research*, *106*, 13,989–14,000. https://doi.org/10.1029/2000jc000518

Madec, G. (2008). NEMO ocean engine. *Tech. Rep. 27*, Institut Pierre Simon Laplace (ISPL).

McLaughlin, F. A., & Carmack, E. C. (2010). Deepening of the nutricline and chlorophyll maximum in the Canada Basin interior, 2003–2009. *Geophysical Research Letters*, *37*, L24602. https://doi.org/10.1029/2010GL045459

McMinn, A., & Hegseth, E. N. (2007). Sea ice primary productivity in the northern Barents Sea, spring 2004. *Polar Biology*, *30*(3), 289–294. https://doi.org/10.1007/s00300-006-0182-x

Michel, C., Legendre, L., Ingram, R. G., Gosselin, M., & Levasseur, M. (1996). Carbon budget of sea-ice algae in spring: Evidence of a significant transfer to zooplankton grazers. *Journal of Geophysical Research*, *101*, 18,345–18,360. https://doi.org/10.1029/96jc00045

Moore, J. K., Doney, S. C., & Lindsay, K. (2004). Upper ocean ecosystem dynamics and iron cycling in a global three-dimensional model. *Global Biogeochemical Cycles*, *18*, GB4028. https://doi.org/10.1029/2004GB002220

Moore, J. K., Lindsay, K., Doney, S. C., Long, M. C., & Misumi, K. (2013). Marine ecosystem dynamics and biogeochemical cycling in the Community Earth System Model (CESM1(BGC)): Comparison of the 1990s with the 2090s under the RCP4.5 and RCP8.5 scenarios. *Journal of Climate*, *26*, 9291–9312. https://doi.org/10.1175/jcli-d-12-00566.1

Mortenson, E., Hayashida, H., Steiner, N., Monahan, A., Blais, M., Gale, M. A., et al. (2017). A model-based analysis of physical and biological controls on ice algal and pelagic primary production in Resolute Passage. *Elementa: Science of the Anthropocene*, *5*, 229. https://doi.org/10.1525/elementa.229

Niemi, A., & Michel, C. (2015). Temporal and spatial variability in sea-ice carbon:nitrogen ratios on Canadian Arctic shelves. *Elementa: Science of the Anthropocene*, *3*, 78. https://doi.org/10.12952/journal.elementa.000078

Nishi, Y., & Tabeta, S. (2005). Analysis of the contribution of ice algae to the ice-covered ecosystem in Lake Saroma by means of a coupled ice-ocean ecosystem model. *Journal of Marine Systems*, *55*, 249–270. https://doi.org/10.1016/j.jmarsys.2004.08.002

Nishino, S., Kiluchi, T., Yamamoto-Kawai, M., Kawaguchi, Y., Hirawake, T., & Itoh, M. (2011). Enhancement/reduction of biological pump depends on ocean circulation in the sea-ice reduction regions of the Arctic Ocean. *Journal of Oceanography*, *67*, 305–314. https://doi.org/10.1007/s10872-011-0030-7

Olsen, A., Key, R. M., van Heuven, S., Lauvset, S. K., Velo, A., Lin, X., et al. (2016). The Global Ocean Data Analysis Project version 2 (GLODAPv2)—An internally consistent data product for the world ocean. *Earth System Science Data*, *8*, 297–323. https://doi.org/10.5194/essd-8-297-2016

Parkinson, C. L., & Cavalieri, D. J. (2008). Arctic sea ice variability and trends, 1979–2006. *Journal of Geophysical Research*, *113*, C07003. https://doi.org/10.1029/2007JC004558

Pickart, R. S. (2004). Shelfbreak circulation in the Alaskan Beaufort Sea: Mean structure and variability. *Journal of Geophysical Research*, *109*, C04024. https://doi.org/10.1029/2003JC001912

Polyakov, I. V., Pnyushkov, A. V., Alkire, M. B., Ashik, I. M., Baumann, T. M., Carmack, E. C., et al. (2017). Greater role for Atlantic inflows on sea-ice loss in the Eurasian Basin of the Arctic Ocean. *Science*, *356*, 285–291. https://doi.org/10.1126/science.aai8204

Popova, E. E., Yool, A., Coward, A. C., Dupont, F., Deal, C., Elliott, S., et al. (2012). What controls primary production in the Arctic Ocean? Results from an intercomparison of five general circulation models with biogeochemistry. *Journal of Geophysical Research*, *117*, C00D12. https://doi.org/10.1029/2011JC007112

Proshutinsky, A., Bourke, R. H., & McLaughlin, F. A. (2002). The role of the Beaufort Gyre in Arctic climate variability: Seasonal to decadal climate scales. *Geophysical Research Letters*, *29*, 2100. https://doi.org/10.1029/2002GL015847

Proshutinsky, A., Krishfield, R., Timmermans, M.-L., Toole, J., Carmack, E., McLaughlin, F., et al. (2009). Beaufort Gyre freshwater reservoir: State and variability from observations. *Journal of Geophysical Research*, *114*, C00A10. https://doi.org/10.1029/2008JC005104

Proshutinsky, A., Steele, M., & Timmermans, M.-L. (2016). Forum for Arctic Modeling and Observational Synthesis (FAMOS): Past, current, and future activities. *Journal of Geophysical Research: Oceans*, *121*, 3803–3819. https://doi.org/10.1002/2016JC011898

Saha, S., Moorthi, S., Pan, H.-L., Wu, X., Wang, J., Nadiga, S., et al. (2010). The NCEP Climate Forecast System reanalysis. *Bulletin of the American Meteorological Society*, *91*, 1015–1057. https://doi.org/10.1175/2010BAMS3001.1

Schollmeier, T., Oliveira, A. C. M., Wooller, M. J., & Iken, K. (2018). Tracing sea ice algae into various benthic feeding types on the Chukchi Sea shelf. *Polar Biology*, *41*(2), 207–224. https://doi.org/10.1007/s00300-017-2182-4

Schweiger, A., Lindsay, R., Zhang, J., Steele, M., Stern, H., & Kwok, R. (2011). Uncertainty in modeled Arctic sea ice volume. *Journal of Geophysical Research*, *116*, C00D06. https://doi.org/10.1029/2011JC007084

Simmonds, I., & Rudeva, I. (2012). The great Arctic cyclone of August 2012. *Geophysical Research Letters*, *39*, L23709. https://doi.org/10.1029/2012GL054259

Spall, M. A., Pickart, R. S., Li, M., Itoh, M., Lin, P., Kikuchi, T., & Qi, Y. (2018). Transport of Pacific water into the Canada Basin and the formation of the Chukchi Slope Current. *Journal of Geophysical Research: Oceans*, *123*, 7453–7471. https://doi.org/10.1029/2018JC013825

Spall, M. A., Pickart, R. S., Fratantoni, P. S., & Plueddemann, A. J. (2008). Western Arctic shelfbreak eddies: Formation and transport. *Journal of Physical Oceanography*, *38*, 1644–1668. https://doi.org/10.1175/2007jpo3829.1

Steele, M., Morley, R., & Ermold, W. (2001). PHC: A global ocean hydrography with a high-quality Arctic Ocean. *Journal of Climate*, *14*, 2079–2087. https://doi.org/10.1175/1520-0442(2001)014<2079:PAGOHW>2.0.CO;2

Steiner, N., Deal, C., Lannuzel, D., Lavoie, D., Massonnet, F., Miller, L. A., et al. (2016). What sea-ice biogeochemical modellers need from observers. *Elementa: Science of the Anthropocene*, *4*, 84. https://doi.org/10.12952/journal.elementa.000084

Steiner, N., & Stefels, J. (2017). Commentary on the outputs and future of Biogeochemical Exchange Processes at Sea-Ice Interfaces (BEPSII). *Elementa: Science of the Anthropocene*, *5*, 81. https://doi.org/10.1525/elementa.272

Steiner, N. S., Sou, T., Deal, C., Jackson, J. M., Jin, M., Popova, E., et al. (2016). The future of the subsurface chlorophyll-a maximum in the Canada Basin—A model intercomparison. *Journal of Geophysical Research: Oceans*, *121*, 387–409. https://doi.org/10.1002/2015JC011232

Tamelander, T., Reigstad, M., Hop, H., & Ratkova, T. (2009). Ice algal assemblages and vertical export of organic matter from sea ice in the Barents Sea and Nansen Basin (Arctic Ocean). *Polar Biology*, *32*, 1261–1273. https://doi.org/10.1007/s00300-009-0622-5

Tedesco, L., Vichi, M., & Scoccimarro, E. (2019). Sea-ice algal phenology in a warmer Arctic. *Science Advances*, *5*, eaav4830. https://doi.org/10.1126/sciadv.aav4830

Tremblay, J.-É., Anderson, L. G., Matrai, P., Coupel, P., Bélanger, S., Michel, C., & Reigstad, M. (2015). Global and regional drivers of nutrient supply, primary production and CO_2 drawdown in the changing Arctic Ocean. *Progress in Oceanography*, *139*, 171–196. https://doi.org/10.1016/j.pocean.2015.08.009

Uppala, S. M., Kållberg, P. W., Simmons, A. J., Andrae, U., Bechtold, V. D. C., Fiorino, M., et al. (2005). The ERA-40 re-analysis. *Quarterly Journal of the Royal Meteorological Society*, *131*, 2961–3012. https://doi.org/10.1256/qj.04.176

van Leeuwe, M. A., Tedesco, L., Arrigo, K. R., Assmy, P., Campbell, K., Meiners, K. M., et al. (2018). Microalgal community structure and primary production in Arctic and Antarctic sea ice: A synthesis. *Elementa: Science of the Anthropocene*, *6*, 4. https://doi.org/10.1525/elementa.267

Vancoppenolle, M., Bopp, L., Madec, G., Dunne, J., Ilyina, T., Halloran, P. R., & Steiner, N. (2013). Future Arctic Ocean primary productivity from CMIP5 simulations: Uncertain outcome, but consistent mechanisms. *Global Biogeochemical Cycles*, *27*, 605–619. https://doi.org/10.1002/gbc.20055

Vancoppenolle, M., Meiners, K. M., Michel, C., Bopp, L., Brabant, F., Carnat, G., et al. (2013). Role of sea ice in global biogeochemical cycles: Emerging views and challenges. *Quaternary Science Reviews*, *79*, 207–230. https://doi.org/10.1016/j.quascirev.2013.04.011

Wang, J., Zhang, J., Watanabe, E., Ikeda, M., Mizobata, K., Walsh, J. E., et al. (2009). Is the Dipole Anomaly a major driver to record lows in Arctic summer sea ice extent? *Geophysical Research Letters*, *36*, L05706. https://doi.org/10.1029/2008GL036706

Warren, S. G., Rigor, I. G., Untersteiner, N., Radionov, V. F., Bryazgin, N. N., Aleksandrov, Y. I., & Colony, R. (1999). Snow depth on Arctic sea ice. *Journal of Climate*, *12*, 1814–1829. https://doi.org/10.1175/1520-0442(1999)012<1814:SDOASI>2.0.CO;2

Watanabe, E., Onodera, J., Harada, N., Aita, M. N., Ishida, A., & Kishi, M. J. (2015). Wind-driven interannual variability of sea ice algal production in the western Arctic Chukchi Borderland. *Biogeosciences*, *12*, 6147–6168. https://doi.org/10.5194/bg-12-6147-2015

Watanabe, E., Onodera, J., Harada, N., Honda, M. C., Kimoto, K., Kikuchi, T., et al. (2014). Enhanced role of eddies in the Arctic marine biological pump. *Nature Communications*, *5*(1), 1–9. https://doi.org/10.1038/ncomms4950

Watanabe, E., Onodera, J., Itoh, M., Nishino, S., & Kikuchi, T. (2017). Winter transport of subsurface warm water toward the Arctic Chukchi Borderland. *Deep-Sea Research Part I*, *128*, 115–130. https://doi.org/10.1016/j.dsr.2017.08.009

Wilchinsky, A. V., & Feltham, D. L. (2004). A continuum anisotropic model of sea-ice dynamics. *Proceedings of the Royal Society of London*, *460*, 2105–2140. https://doi.org/10.1098/rspa.2004.1282

Woodgate, R. A., Aagaard, K., & Weingartner, T. J. (2005). Monthly temperature, salinity, and transport variability of the Bering Strait through flow. *Geophysical Research Letters*, *32*, L04601. https://doi.org/10.1029/2004GL021880

Yamamoto-Kawai, M., McLaughlin, F. A., & Carmack, E. C. (2011). Effects of ocean acidification, warming and melting of sea ice on aragonite saturation of the Canada Basin surface water. *Geophysical Research Letters*, *38*, L03601. https://doi.org/10.1029/2010GL045501

Zhang, J., Ashjian, C., Campbell, R., Spitz, Y. H., Steele, M., & Hill, V. (2015). The influence of sea ice and snow cover and nutrient availability on the formation of massive under-ice phytoplankton blooms in the Chukchi Sea. *Deep–Sea Research Part II*, *118*, 122–135. https://doi.org/10.1016/j.dsr2.2015.02.008

Zhang, J., & Rothrock, D. A. (2003). Modeling global sea ice with a thickness and enthalpy distribution model in generalized curvilinear coordinates. *Monthly Weather Review*, *131*, 845–861. https://doi.org/10.1175/1520-0493(2003)131<0845:MGSIWA>2.0.CO;2

Zhang, J., Spitz, Y. H., Steele, M., Ashjian, C., Campbell, R., Berline, L., & Matrai, P. (2010). Modeling the impact of declining sea ice on the Arctic marine planktonic ecosystem. *Journal of Geophysical Research*, *115*, C10015. https://doi.org/10.1029/2009JC005387

Zhang, J., & Steele, M. (2007). Effect of vertical mixing on the Atlantic Water layer circulation in the Arctic Ocean. *Journal of Geophysical Research*, *112*, C04S04. https://doi.org/10.1029/2006JC003732